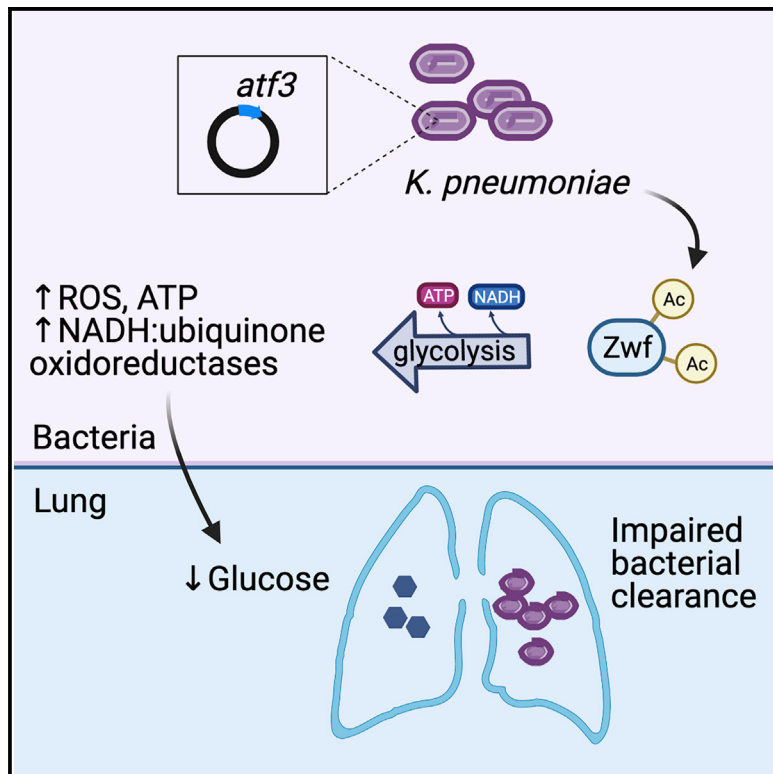


An acquired acyltransferase promotes *Klebsiella pneumoniae* ST258 respiratory infection

Graphical abstract



Authors

Danielle Ahn, Gitanjali Bhushan,
Thomas H. McConville, ...,
Robert K. Ernst, Anne-Catrin Uhlemann,
Alice Prince

Correspondence

dsa2120@cumc.columbia.edu

In brief

Klebsiella pneumoniae ST258 is a successful human pathogen. Here, Ahn et al. identify an acyltransferase of the superfamily 3 (*atf3*) concentrated within one of the ST258 clades. Acquisition of this gene leads to enhanced bioenergetic properties, giving the pathogen a competitive advantage *in vivo*.

Highlights

- An acyltransferase (*atf3*) is prevalent in ST258 *K. pneumoniae*
- Expression of *atf3* enhances glycolysis, increasing bacterial ATP production and ROS
- With *atf3*, the airway metabolome was altered with greater glucose consumption
- *K. pneumoniae* expressing *atf3* has a competitive advantage *in vivo*



Article

An acquired acyltransferase promotes *Klebsiella pneumoniae* ST258 respiratory infection

Danielle Ahn,^{1,5,*} Gitanjali Bhushan,¹ Thomas H. McConville,² Medini K. Annavajhala,² Rajesh Kumar Soni,³ Tania Wong Fok Lung,¹ Casey E. Hofstaedter,⁴ Shivang S. Shah,¹ Alexander M. Chong,² Victor G. Castano,¹ Robert K. Ernst,⁴ Anne-Catrin Uhlemann,² and Alice Prince¹

¹Department of Pediatrics, Columbia University Irving Medical Center, New York, NY 10032, USA

²Department of Medicine, Columbia University Irving Medical Center, New York, NY 10032, USA

³Proteomics and Macromolecular Crystallography Shared Resource, Herbert Irving Comprehensive Cancer Center, Columbia University Irving Medical Center, New York, NY 10032, USA

⁴Department of Microbial Pathogenesis, University of Maryland, Baltimore, Baltimore, MD 21201, USA

⁵Lead contact

*Correspondence: dsa2120@cumc.columbia.edu

<https://doi.org/10.1016/j.celrep.2021.109196>

SUMMARY

Klebsiella pneumoniae ST258 is a human pathogen associated with poor outcomes worldwide. We identify a member of the acyltransferase superfamily 3 (*atf3*), enriched within the ST258 clade, that provides a major competitive advantage for the proliferation of these organisms *in vivo*. Comparison of a wild-type ST258 strain (KP35) and a $\Delta atf3$ isogenic mutant generated by CRISPR-Cas9 targeting reveals greater NADH:ubiquinone oxidoreductase transcription and ATP generation, fueled by increased glycolysis. The acquisition of *atf3* induces changes in the bacterial acetylome, promoting lysine acetylation of multiple proteins involved in central metabolism, specifically Zwf (glucose-6 phosphate dehydrogenase). The *atf3*-mediated metabolic boost leads to greater consumption of glucose in the host airway and increased bacterial burden in the lung, independent of cytokine levels and immune cell recruitment. Acquisition of this acyltransferase enhances fitness of a *K. pneumoniae* ST258 isolate and may contribute to the success of this clonal complex as a healthcare-associated pathogen.

INTRODUCTION

Multi-drug-resistant Gram-negative pathogens are an increasing threat, limiting the effectiveness of even novel therapeutic strategies (Doi et al., 2017). These organisms are an omnipresent complication of modern intensive care unit (ICU) care, causing ventilator-associated pneumonia (Cillóniz et al., 2019), superinfection following viral illnesses such as severe acute respiratory syndrome-coronavirus-2 (SARS-CoV-2) (Gomez-Simmonds et al., 2020), and bloodstream infections (Satlin et al., 2017). Carbapenem-resistant *Klebsiella pneumoniae* (CRKP) is among the current epidemic of multi-drug-resistant Gram-negative bacteria associated with unacceptably high morbidity and mortality (Borer et al., 2009; Kohler et al., 2017; Xu et al., 2017). Within CRKP, the sequence type 258 (ST258) has emerged as a persistent and overrepresented cause of hospital-associated infections in the United States and worldwide (Marsh et al., 2019; Tzouvelekis et al., 2013; van Duin et al., 2020). Transposon screens have been used to identify loci that promote *K. pneumoniae* pathogenicity (Bachman et al., 2015; Paczosa et al., 2020; Vornhagen et al., 2019). However, such studies typically use a laboratory reference isolate (American Type Culture Collection [ATCC] 43816 or KPPR1), which is genetically distinct from the highly anti-

biotic resistant ST258 clonal complex (Gomez-Simmonds and Uhlemann, 2017; Vornhagen et al., 2019). To understand the bacterial properties responsible for the success of *K. pneumoniae* ST258, we analyzed clinical isolate 35 (KP35) from our own hospital, a representative strain that expresses the most common cps (capsular protein) and wzi (capsular component) genotypes (Ahn et al., 2016; Gomez-Simmonds et al., 2015). The median lethal dose (LD_{50}) of ST258 isolates is several logs higher than KPPR1 (Xiong et al., 2015), consistent with our previous work in which a much higher inoculum of KP35 was required to induce pathology in a murine model of pneumonia (Ahn et al., 2016). KP35 displayed kinetics of infection similar to what has been observed in humans—an indolent but progressive pneumonia characterized by the recruitment of anti-inflammatory monocytes that fail to clear infection and are typically present in the resolution phase of infection (Poe et al., 2013). The influx of these monocytes in response to infection with ST258 strains then elicits a subdued immune response mediated by interleukin-10 (IL-10) secretion (Peñaloza et al., 2019).

The genetic elements responsible for the global persistence of ST258 *K. pneumoniae* have not been identified (Tzouvelekis et al., 2013). The prevailing wisdom suggests that the acquisition of antimicrobial resistance elements carries a fitness cost that is



often not detected under *in vitro* conditions (Wong et al., 2019). This fitness cost is predicted to lead to reversibility in the absence of antimicrobial pressure (Andersson and Hughes, 2010; Bachman et al., 2015) and is the foundation for the development of antimicrobial stewardship programs. However, the dissemination and persistence of ST258 organisms worldwide, amidst many other species of opportunistic pathogens, implies that they may have other properties to promote selection *in vivo* (Ernst et al., 2020). Comprehensive genotypic and phenotypic studies of ST258 isolates have identified interesting but inconsistent virulence determinants such as those involved in iron utilization, stress response signaling, biofilm formation, and type IV pili (Marsh et al., 2019; Pitout et al., 2015). In the absence of a unifying virulence phenotype, it has been postulated that the dynamic evolution of these mechanisms of persistence within the host microbiota is due to the availability of metabolites generated by recruited immune cells as well as by bacteria (Blin et al., 2017; Vornhagen et al., 2019). We hypothesized that the success of pathogens like ST258 *K. pneumoniae* could also be attributable to less apparent factors such as the metabolic properties of the bacteria.

In the KP35 genome, we identified an open reading frame (ORF) that provides KP35 with a selective advantage, enhancing persistence in the murine lung (Ahn et al., 2016). This ORF, initially designated in our previous publication as an arginine antiporter (*arcD*), is now annotated *in silico* as a member of the acyltransferase superfamily 3 (*atf3*), a diverse group of proteins linked to metabolic pathways. In the experiments detailed here, we show that this element promotes a global increase in *K. pneumoniae* bioenergetics with increased ATP production through enhanced glycolysis and tricarboxylic acid (TCA) cycle activity, leading to increased substrate utilization and persistent pulmonary infection. This augmented metabolic activity may negate the metabolic expense of maintaining antibiotic resistance genes and provide KP35 with a metabolic boost that contributes to its persistence in the lung.

RESULTS

Acquisition of an acyltransferase superfamily 3 (*atf3*) is ubiquitous in an ST258 clade

We determined whether the unique ORF in KP35, annotated *in silico* as a member of the acyltransferase superfamily 3 (*atf3*) and previously associated with increased fitness in a murine model of pneumonia (Ahn et al., 2016), was present across diverse *K. pneumoniae* clones. Phylogenetic reconstruction of the 178 publicly available genomes in NCBI showed that *atf3* was only present in ST258 isolates (Figure 1A), appreciating that the data from sequenced isolates may be skewed toward those associated with clinically important infections or hospital outbreaks. In phylogenetic analyses focused on only ST258 isolates ($n = 100$), we found that *atf3* is concentrated in clade 1, one of the two major ST258 clades that expresses KPC-2 and *wzi* 29, although we observed some isolates with a sporadic loss of the gene (Figure 1B). Of note, *atf3* was not present in KPPR1, the laboratory reference strain often used in studies of *K. pneumoniae* pathogenicity. The 332-amino acid protein encoded by *atf3* is predicted *in silico* to be a transmembrane protein, but lacks ho-

mology with known proteins. Phylogeny of *atf3* members as represented in a sunburst diagram (Pfam), demonstrating the ubiquity and heterogeneity of this ancient enzyme domain across 6,022 species (Figure 1C).

Deletion of *atf3* does not alter the physical properties of KP35

Neither the primary sequence nor the predicted protein structure of the KP35 *atf3* gene product indicates its function. However, *atf3* is colocated with multiple genes involved in capsular production (*ugd*, *gnd*; components of the *cps* cluster in *K. pneumoniae*) (Pan et al., 2015) and O-antigen synthesis (*wbgU*, *tagGH*) (Bruchmann et al., 2021; Caboni et al., 2015) (Figure 2A). To study the role of *atf3* in pathogenesis, a null mutant was constructed using a recently adapted CRISPR-Cas9 system, Lambda Red Recombineering genes to improve efficiency, and Zeocin selection due to the presence of multiple antimicrobial resistance elements in the KP35 genome (McConvile et al., 2020). A 122-bp deletion beginning 4 bp upstream of the start codon was confirmed by whole-genome sequencing. The deletion mutant was complemented with a cloned version of *atf3* expressed on a high copy number plasmid under Zeocin selection. The basic properties of the three strains were compared *in vitro* and found to have equivalent rates of growth in Luria-Bertani (LB) media (Figure 2B), formation of biofilm (Figure S1A), and susceptibility to antimicrobials (Figure S1B).

Among the many functions ascribed to *K. pneumoniae* acyltransferases, modification of the lipid A component of lipopolysaccharide (LPS) is a potential mechanism that could affect pathogenesis. Using MALDI-TOF mass spectrometry, we established that WT KP35 and the $\Delta atf3$ mutant did not have major differences in LPS lipid A structure (Figures 2C and 2D). However, there was an increased abundance of LPS O-antigen side chains and core protein in the $\Delta atf3$ mutant (Figures S2C and S2D). These differences in LPS did not translate into altered susceptibility to polymyxin B or H_2O_2 (Figures S1B and S1E). These findings indicated that *atf3* is conserved within the ST258 *K. pneumoniae* clonal clade and that its deletion did not significantly change the baseline characteristics of this clinical isolate.

The presence of *atf3* increases *K. pneumoniae* glycolysis and TCA cycle activity

The impact of *atf3* on KP35 gene expression was assessed by RNA sequencing (RNA-seq) comparing KP35 and the $\Delta atf3$ mutant grown in LB broth overnight (Figure 3A). Kyoto Encyclopedia of Genes and Genomes (KEGG) pathway analysis of the top 50 genes with increased expression in KP35 as compared to the $\Delta atf3$ mutant showed the upregulation of many metabolic pathways, suggesting that *atf3* activity is primarily involved in enhancing the ability of KP35 to generate energy (Figure 3B). This was reflected in the increased expression of glycolytic enzymes in WT KP35 compared to the $\Delta atf3$ mutant, and to a lesser extent in the components of the TCA cycle (Figure 3C). To determine the possible role of *atf3* acyltransferase activity in bacterial metabolism, we compared the assimilation of single carbon sources that are intermediate steps in glycolysis and the TCA cycle. There was preferential metabolism of glucose and glycolytic intermediates in minimal media by KP35, as determined by the

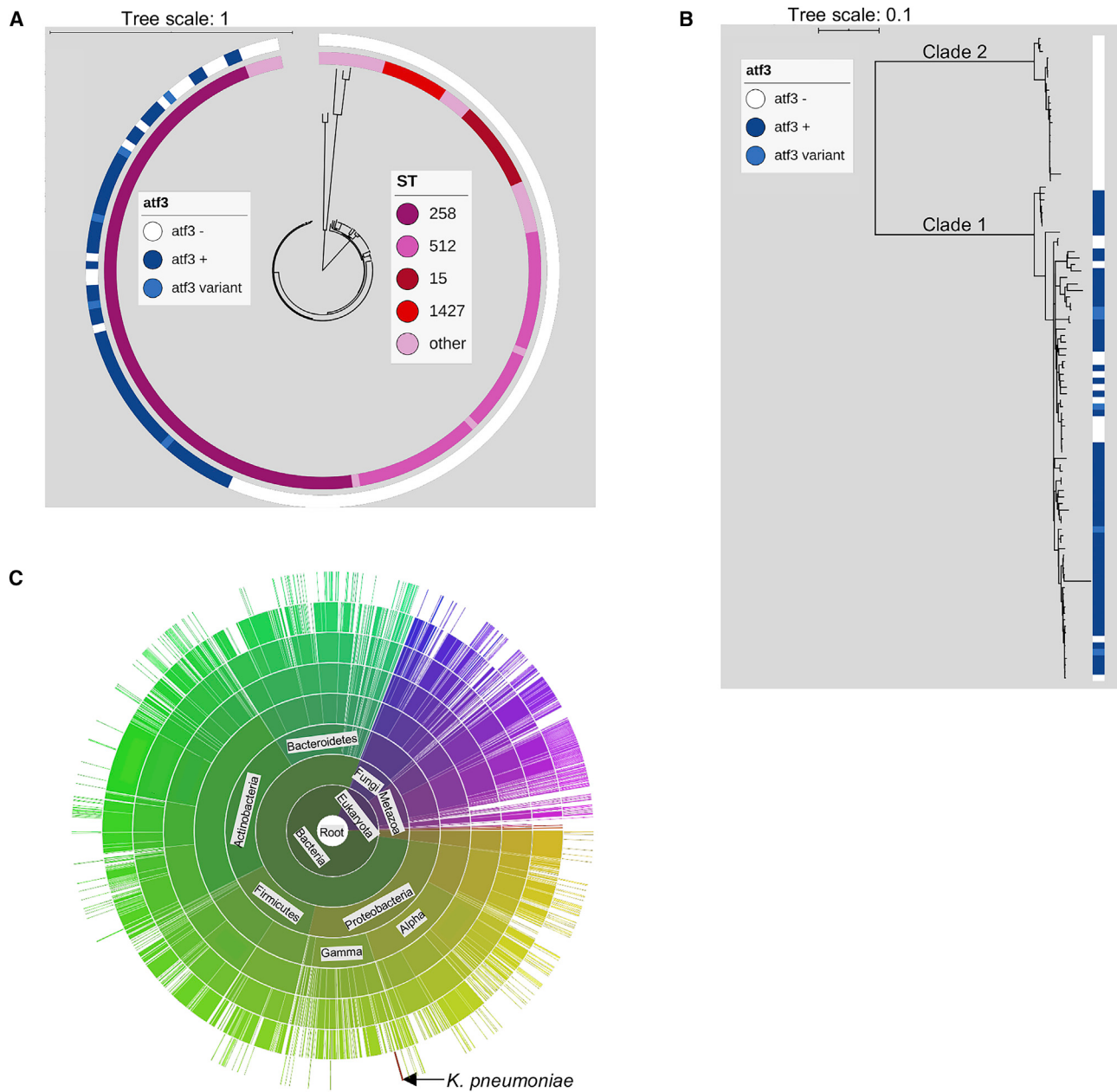


Figure 1. A novel acyltransferase of the superfamily 3 (atf3) is prevalent in *K. pneumoniae* ST258 isolates

(A) A phylogenetic tree of the publicly available assemblies of *K. pneumoniae* isolates. The inner ring represents the ST group to which the isolate belongs and the outer ring is the screen for the *atf3* gene, with isolates designated as a variant if it contained at least 1 point mutation.

(B) A concentrated phylogenetic tree of ST258 isolates only.

(C) A sunburst visualization of species, considering taxonomic lineage, with members of the acyltransferase superfamily 3.

reduction of tetrazolium blue, relative to the Δ *atf3* mutant or the laboratory standard KPPR1, included for comparison (Figure 3D). Static growth in minimal media with increasing concentrations of selected metabolites showed no major differences in growth to explain this difference (Figures S2A–S2D). In RPMI, a more nutrient-rich media, growth of the bacteria with differing concentrations of glucose was similar for WT KP35 and Δ *atf3* (Figure S2E).

There was enhancement in the glycolytic activity of KP35 alone as compared to Δ *atf3*. Using the Seahorse analyzer, we observed relatively higher extracellular acidification rates (ECARs) of KP35 in response to glucose to initiate glycolysis and to oligomycin to block oxidative phosphorylation and unleash glycolytic capacity (Figure 3E). The expected reduction in glycolytic activity by 2-deoxyglucose was observed for both bacterial strains. A relative increase in oxygen consumption

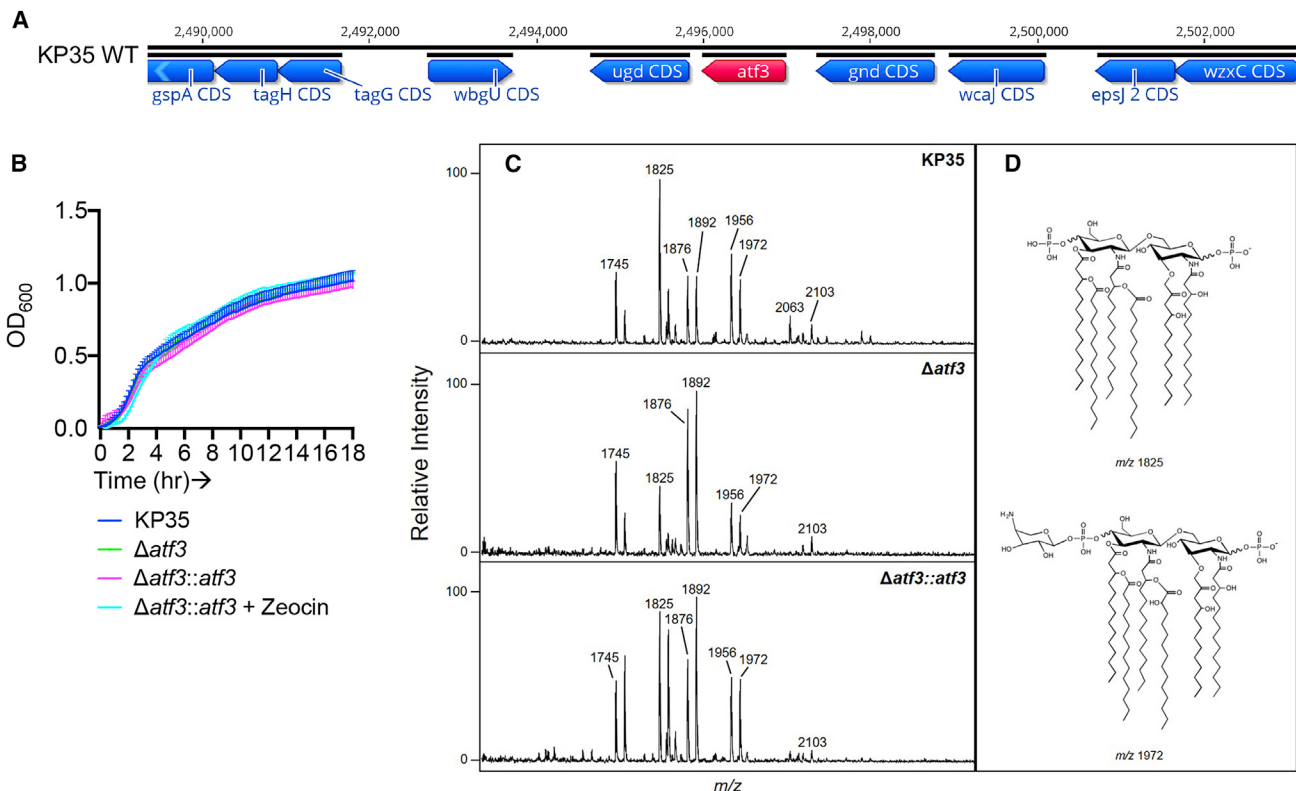


Figure 2. The growth rate and lipid A structure for KP35 are unchanged with the deletion of the *atf3* gene

(A) Schematic of the KP35 *atf3* gene locus using Geneious version 10.

(B) Serial optical density at wavelength of 600 nm (OD₆₀₀) measurements of bacteria were taken over 18 h with intermittent shaking at 37°C in LB. n = 3; each point is the mean value, with bars representing the SEMs.

(C) Negative ion mode MALDI-TOF MS lipid A spectra are shown for KP35, Δ*atf3*, and Δ*atf3::atf3* (n = 1). The strains were grown at 37°C in LB for 18 h. Additions of a hydroxyl group (Δm/z 16) and an aminoarabinose group (Δm/z 131) are observed among all 3 strains. The ion at m/z 1972 demonstrates both modifications. In addition, loss of a phosphate (Δm/z 80) is likely a result of harsh lipid A extraction conditions. The ion at m/z 2063 represents the addition of a palmitate (C16, Δm/z 238) acyl chain.

(D) Representative structures are shown for the ions at m/z 1825 and m/z 1972. The ion at m/z 1956/1972 represents lipid A species with the addition of 1 aminoarabinose moiety, whereas the ion at m/z 2103 represents the addition of 2 aminoarabinose moieties.

rates (OCRs) was also observed in response to glucose in the parent strain (Figure 3F). Of note, these changes in bacterial metabolism did not significantly alter the cumulative host and pathogen metabolic activity as measured in differentiated monocytes (THP-1s) co-incubated with the bacterial strains (Figures 3G and 3H). The expected consequences of heightened metabolism in the presence of *atf3* were documented by the increased generation of reactive oxygen species (ROS) (Figure 3I) and levels of ATP produced by bacteria alone (Figure 3J). This was further supported by the enhanced transcription of virtually all of the *nuo* and *nqr* genes in the parent strain compared to the mutant. These loci encode the individual NADH:ubiquinone oxidoreductase (NQO) components of complex I (Figures 3K and 3L). All 12 of the proton-translocating NQO components (*nuoB*, -C, -E, -F, -G, -H, -I, -J, -K, -L, -M, and -N) were upregulated in the parent strain with *atf3* as were the 6 Na⁺-translocating NQOs (*nqrA*, -B, -C, -D, -E, and -F). These membrane-associated proton (or Na⁺) pumps couple the oxidation of NADH to the reduction of ubiquinone, generate the transmembrane elec-

trochemical gradient, and drive ATP synthesis for bacteria, sharing many essential properties with complex I of mitochondria (Dibrov et al., 2017; Erhardt et al., 2012). The importance and complexities of these NQOs in bacterial energetics has made them a major focus of research for decades (Dimroth, 1987), although a role in pathogenesis has not been specifically described.

Global lysine acetylation of bacterial proteins is increased by *atf3*

Having established a major impact of *atf3* on the expression of metabolic genes by KP35, we hoped to identify the target(s) of the acyltransferase more specifically. In bacteria, post-translational modification of proteins, specifically lysine acetylation, is a major mechanism of metabolic regulation (Christensen et al., 2019b). Acetyl phosphate and acetyl-coenzyme A (CoA), act as donors and can non-enzymatically acetylate proteins, a process that is dependent upon glucose availability and glycolytic activity (Christensen et al., 2019b). Glycolytic and TCA cycle

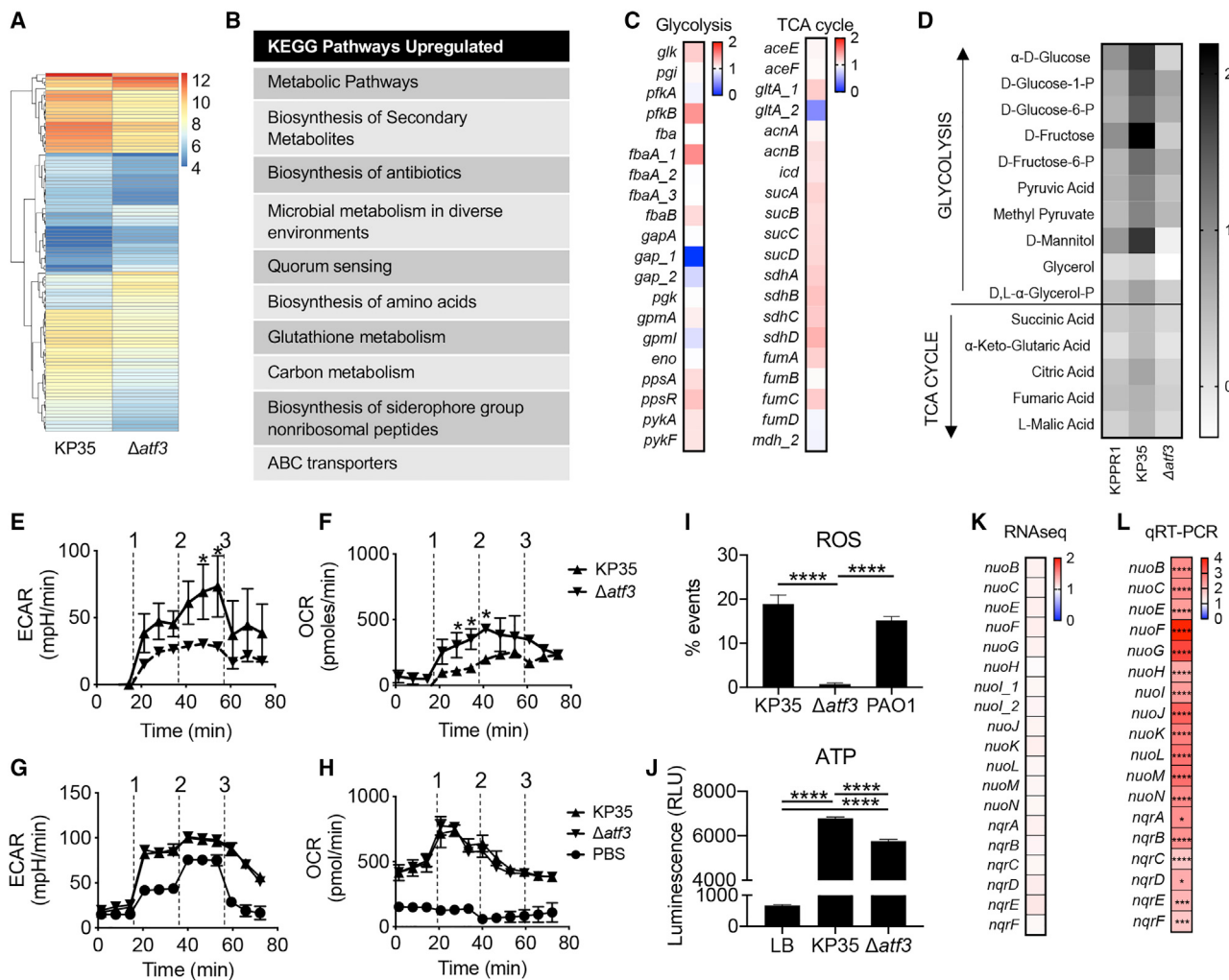


Figure 3. Enhanced metabolic properties of *K. pneumoniae* ST258 in the presence of *atf3*.

(A) Shotgun RNA-seq of bacteria alone, Illumina platform, heatmap of variance stabilized counts. n = 1.

(B) KEGG pathway analysis showing the top 10 pathways increased in KP35 with respect to the isogenic mutant.

(C) Heatmap of the fold expression of the genes involved in glycolysis and TCA cycle enzymes expressed by KP35 over Δatf3 (n = 1).

(D) Single carbon source assimilation (Biolog) (n = 2). KPPR1 = laboratory reference strain ATCC 43816.

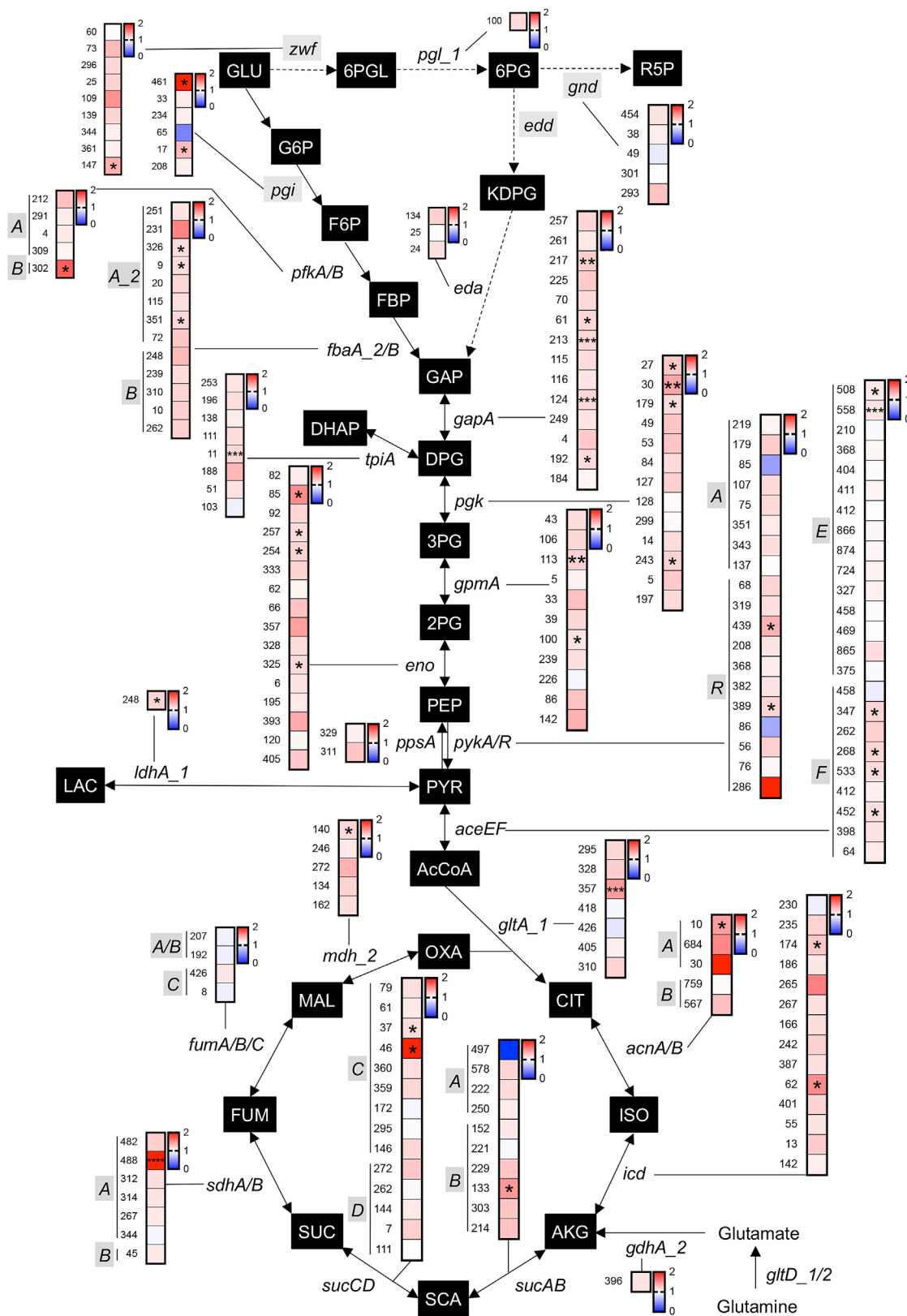
(E–H) Glycolysis as measured by (E) extracellular acidification rates (ECARs) and (F) oxygen consumption rates (OCRs) as measured by Seahorse analyzer of bacteria alone (n = 4) and (G) and (H) with THP1 s (n = 5). 1 = glucose, 2 = oligomycin, 3 = 2-deoxyglucose; each point is the mean value with bars representing the SEM; *p < 0.05 between KP35 and Δatf3, 2-way ANOVA.

(I–K) Intracellular reactive oxygen species (ROS) measured by MitoSOX (Invitrogen) dye via flow cytometry (n = 4) (I). (J) Total ATP production (Abcam) (n = 8). For (I) and (J), columns are mean values with bars representing the SEM; ***p < 0.001, 1-way ANOVA, Tukey's test for multiple comparisons. Heatmap of the fold expression of the Na-independent and -dependent NADH:quinone oxidoreductases expressed by KP35 over Δatf3 via (K) RNA-seq (n = 1) and confirmed with standard qRT-PCR (n = 3, 2 technical replicates per sample).

*p < 0.05, **p < 0.01, ***p < 0.005, ****p < 0.001; multiple t tests with a false discovery rate (FDR) of 1%.

enzymes are among the most frequent targets for lysine acetylation (Nakayasu et al., 2017). We postulated that either the metabolic consequences of *atf3* with increased availability of acetyl-CoA or acetyl phosphate or possibly a specific Atf3 target could lead to changes in the lysine acetylation of key metabolic enzymes. Acetyl-lysine motifs on bacterial proteins were captured using an immunoaffinity bead kit and abundance measured via tandem mass spectrometry (MS/MS) (Figure 4). KP35 exhibited substantially increased site-specific acetylation of many of the

enzymes involved in glycolysis as well as the TCA cycle, as compared with the Δatf3 mutant. Special attention was taken to understand the role of Zwf (glucose-6 phosphate dehydrogenase), Pgi (glucose-6-phosphate isomerase), Edd (phosphogluconate dehydratase), and Gnd (6-phosphogluconate dehydrogenase), as these enzymes are the metabolic switchboard for glucose utilization (Callura et al., 2012). Among the 4 proteins, only Zwf and Pgi had a statistically significant increase in site-specific lysine acetylation, with no modifications measured in



(legend on next page)

Edd. The enzyme Zwf is an important regulator of glucose consumption catalyzing the oxidation of glucose-6 phosphate (glucose-6P) to 6-phosphogluconic acid, a substrate for the Entner-Doudoroff and pentose phosphate pathways. Pgi converts glucose-6P to fructose-6P, the first step in the Embden-Meyerhof pathway, also known as glycolysis. The acetylation of proteins like Zwf and Pgi generally leads to decreased enzymatic activity and would therefore decrease the generation of 6-phosphogluconic acid and fructose-6P, respectively (Nakayasu et al., 2017). Exactly how lysine acetylation affects protein function and whether critical sites for dimerization or the active site itself is modified can be established for enzymes with solved structures. However, since the structure of Zwf and Pgi in KP35 is unknown, we can only demonstrate the likelihood that this critical regulator of glucose metabolism is altered in bacteria expressing *atf3*.

Intracellular metabolite accumulation in KP35 represents diminished Zwf activity and enhanced glycolysis

To demonstrate the impact of *atf3* on bacterial glycolysis, targeted intracellular metabolomics was performed on KP35 and the $\Delta atf3$ mutant (Figure 5A). An increase in the intracellular ADP:ATP ratio in KP35 was consistent with enhanced glycolysis (Figure 5B). There was relative depletion of ATP inside KP35 as compared to the mutant, contrary to our previous observation that total ATP levels were increased in the presence of *atf3* (Figure 3J). This suggests greater movement of ATP extracellularly in the parent strain. Glucose utilization was differential, with its diversion toward the generation of 6-phosphogluconic acid in the $\Delta atf3$ mutant without an increase in other components of the pentose phosphate pathway (Figure 5C). This reduced generation of 6-phosphogluconic acid in KP35 suggests reduced Zwf activity, the expected effect of increased lysine acetylation of the enzyme (Figure 4). In line with the enhanced glycolytic activity previously observed, glucose-6P and fructose-6P levels were relatively elevated within WT KP35 (Figure 5D). While a significant reduction in fructose-6P due to the acetylation of Pgi in the parent strain was not observed, the absolute difference in peak metabolite height (PMH) was reduced between glucose-6P (3.656×10^6 versus 2.873×10^6 , wild-type (WT) KP35 versus $\Delta atf3$) and fructose-6P (1.396×10^6 versus 1.155×10^6 , WT KP35 versus $\Delta atf3$), suggesting the relatively reduced production of fructose-6P in KP35.

Reduced levels of α -ketoglutarate derived from glutamic acid were also measured in the parent strain (Figure 5E). In *Escherichia coli*, α -ketoglutarate alongside glutamine signals the availability of carbon and nitrogen, respectively, for metabolic processes (Doucette et al., 2011). As α -ketoglutarate accumulates, as in the case of the mutant lacking *atf3*, glycolysis is suppressed through the inhibition of enzyme 1, a complex of proteins that transport and phosphorylate glucose as it is taken

up into the cell (Doucette et al., 2011). This feedback mechanism allows the bacteria to sense lower nitrogen availability as α -ketoglutarate is the direct carbon product of nitrogen assimilation through glutamate synthesis. These processes support a role for the *atf3* gene in promoting enhanced utilization of the glycolytic pathway, although a single target for enhanced enzymatic activity is not defined.

Airway metabolomics reflect the consequences of *atf3* on glucose consumption

We next wanted to determine whether the infected airway metabolome similarly reflected the impact of *atf3* on KP35 metabolic activity *in vivo*. We found significant depletion of glucose in KP35 infection relative to the uninfected airway; much less so in $\Delta atf3$ infection (Figure 6A). We then performed a targeted metabolomic analysis of the bronchoalveolar lavage fluid (BALF) harvested from mice infected with either KP35 or the $\Delta atf3$ mutant (Figures 6B and 6C), representing the combined host and bacterial extracellular metabolic environment. At 48 h of infection, the respective metabolomes diverged by principal-component analysis (PCA). There was again a relative depletion of glucose and accumulation of pyruvate in KP35 infection as compared to $\Delta atf3$ (Figure 6D). This is consistent with increased bacterial glycolytic activity and enhanced glucose consumption in the airway. Measurable TCA cycle intermediates were not statistically different from the PBS control (Figure 6E). Among other major metabolites, carnitine was the only compound to be relatively depleted in KP35 infection compared to the $\Delta atf3$ mutant (Figures 6F–6H). The *in vivo* data support the hypothesis that *atf3* contributes to substrate utilization and subsequent energy production, providing a metabolic advantage that may benefit KP35 and its survival in the host lung.

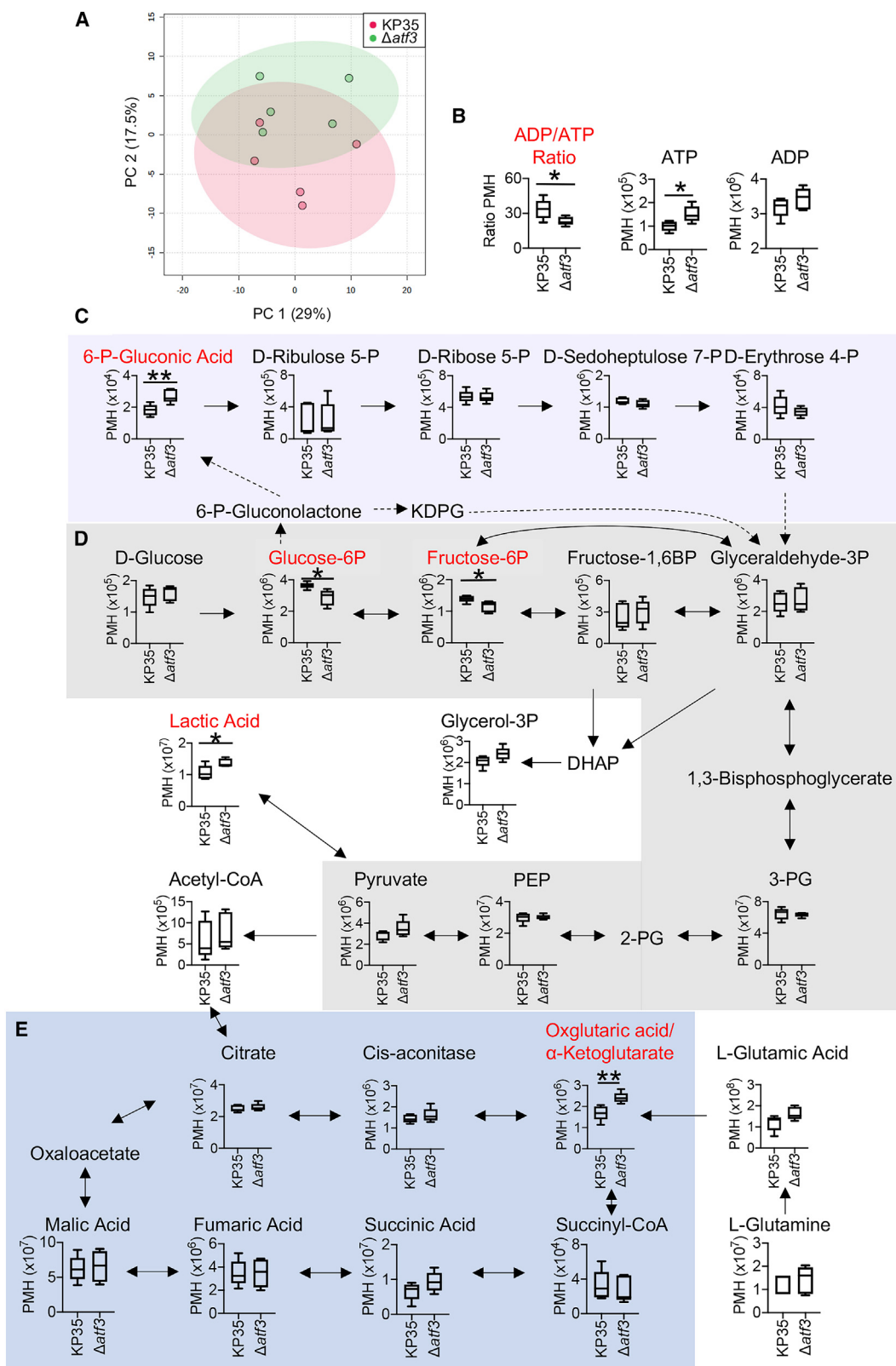
The presence of *atf3* provides a competitive advantage *in vivo*

We next addressed whether the increased metabolic activity associated with *atf3* expression in KP35 contributes to its pathogenicity. We performed a competitive index experiment in a murine model of pneumonia, varying the relative amounts of KP35 and $\Delta atf3$ mutant strain inoculated, to determine whether *atf3* provides a fitness advantage in the lung. The recovery of KP35 from the BALF was significantly greater regardless of increasing proportions of $\Delta atf3$ (Figure 7A). We also observed greater recovery of WT KP35 from the lungs at 48 h post-infection as compared to the $\Delta atf3$ mutant, with similar findings observed for the complemented strain $\Delta atf3::atf3$ (Figure 7B). The persistence of KP35 *in vivo* was demonstrated by the increased number of mice with measurable KP35 colony-forming units (CFU) in the BALF at 168 h post-infection (Figure 7C). We also noted more prominent disruption of the lung architecture with KP35 infection as

Figure 4. Post-translational acetylation of glycolysis and TCA cycle enzymes are increased in the presence of *atf3*

Acetyl-lysine motifs of KP35 and the isogenic mutant were captured with an immunoaffinity bead kit (Cell Signaling). Tandem liquid chromatography/mass spectrometry (LC/LC/MS) was then performed to measure the abundance of acetylation motifs at unique positions (row label) of detected proteins. Heatmaps represent fold abundance of KP35 as compared to the isogenic mutant, with statistically significant differences represented with stars within specific boxes (n = 5).

*p < 0.05, **p < 0.01, ***p < 0.005, ****p < 0.001; multiple t tests with a FDR of 1%. Student's t test performed for datasets with a single acetylation site. Proteins highlighted in gray boxes are members of the metabolic switchboard for glucose utilization.



(legend on next page)

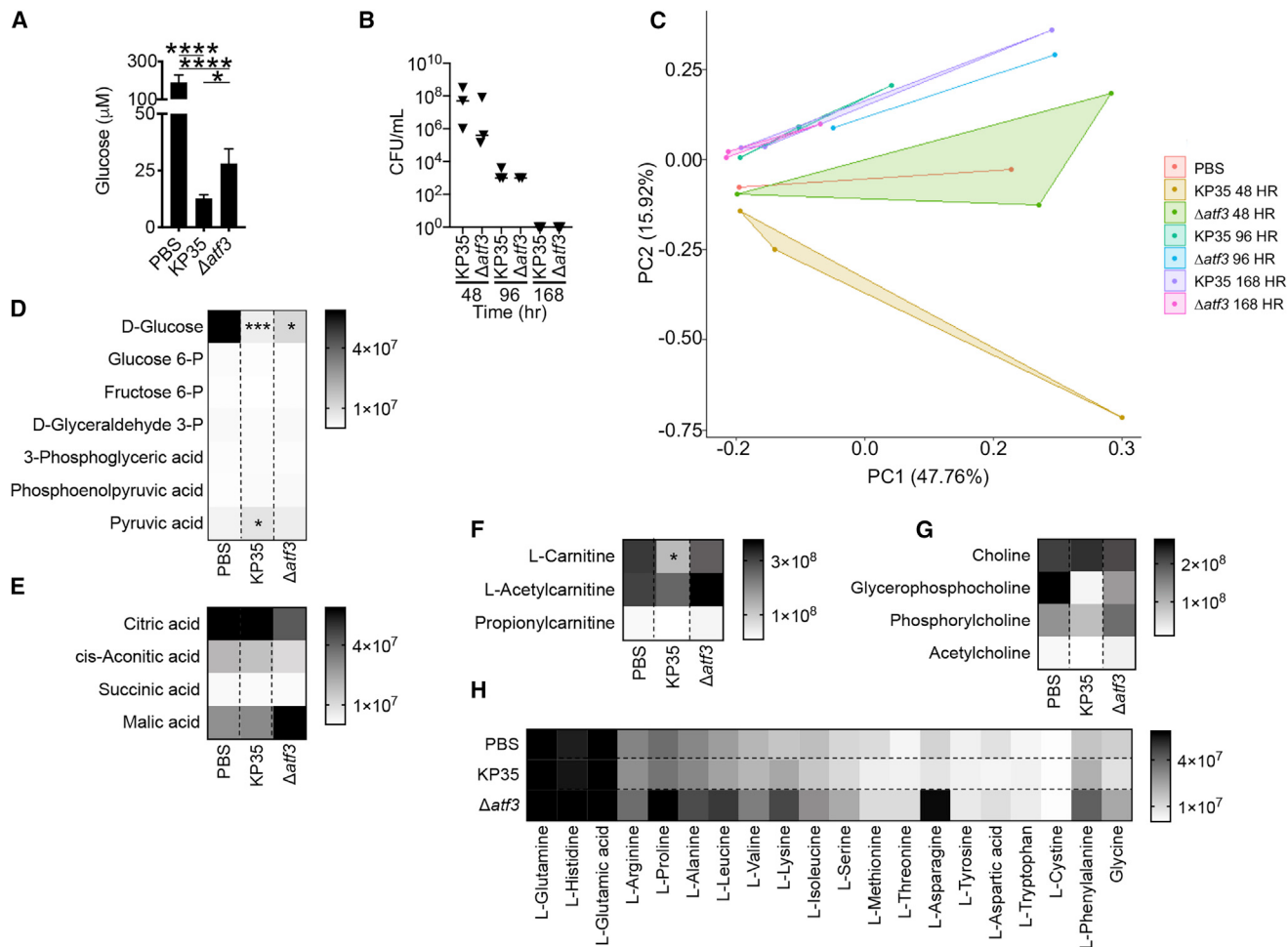


Figure 6. The presence of *atf3* alters the airway metabolome in KP35 infection

WT C57BL/6J mice were intranasally infected with $1-2 \times 10^8$ CFU.

(A) Glucose levels measured in BALF of WT mice infected for 48 h via calorimetric assay (Abcam). n = 5 (PBS) or 9–10 (infected); columns are mean values with bars representing SEM; p < 0.05 (Mann-Whitney), ***p < 0.0001 (one-way ANOVA, Tukey's test for multiple comparisons); recovered CFUs are shown in Figure 7B.

(B) Bacterial CFU recovered from BALF of infected mice over a time course of infection.

(C) PCA plot for metabolites measured from the BALF supernatant of these mice via targeted LC/MS of polar metabolites (n = 2–3, each point represents 1 mouse).

(D–H) Selected peak metabolite levels involved in (D) glycolysis, (E) TCA cycle, (F) carnitine-related metabolites, (G) choline-related metabolites, and (H) amino acids measured in BALF at 48 h of infection are shown via heatmap.

*p < 0.05, ***p < 0.005; multiple t tests with a FDR of 1%, compared to PBS control.

compared to Δatf3 by histopathology (Figure 7D). The immune response to infection did not appear to account for the differences in bacterial recovery. The secreted cytokines in BALF were not significantly different in the WT KP35 or Δatf3 infection (Figures 7E, 7F, and S3), as may be predicted by the absence of major changes in LPS. The numbers of immune cells recovered were also similar (Figure 7G). In vitro assays using differentiated monocytes (THP-1s) confirmed no differences in bacterial uptake and killing (Figure 7H).

DISCUSSION

It has been difficult to explain the prevalence of ST258 *K. pneumoniae* as major healthcare-associated pathogens worldwide beyond their antimicrobial resistance, a feature shared by many other healthcare-associated pathogens. We propose that one factor in their success is the acquisition of a novel acyltransferase, *atf3*, a metabolically enhancing protein that provides a significant growth advantage *in vivo* over bacteria

Figure 5. Accumulation of intracellular metabolites in KP35 reflect enhanced glycolysis and TCA cycle activity when *atf3* is present

(A) PCA plot of targeted polar intracellular bacterial metabolites measured by LC/MS. n = 5, each point represents a biologic replicate.

(B–E) Individual metabolites (B) ATP/ADP, (C) pentose phosphate pathway (purple), (D) glycolysis (gray), and (E) the TCA cycle (blue) were then compared (n = 5). Box and whisker plots with min/max.

*p < 0.05, **p < 0.01; multiple t tests with FDR of 1%.

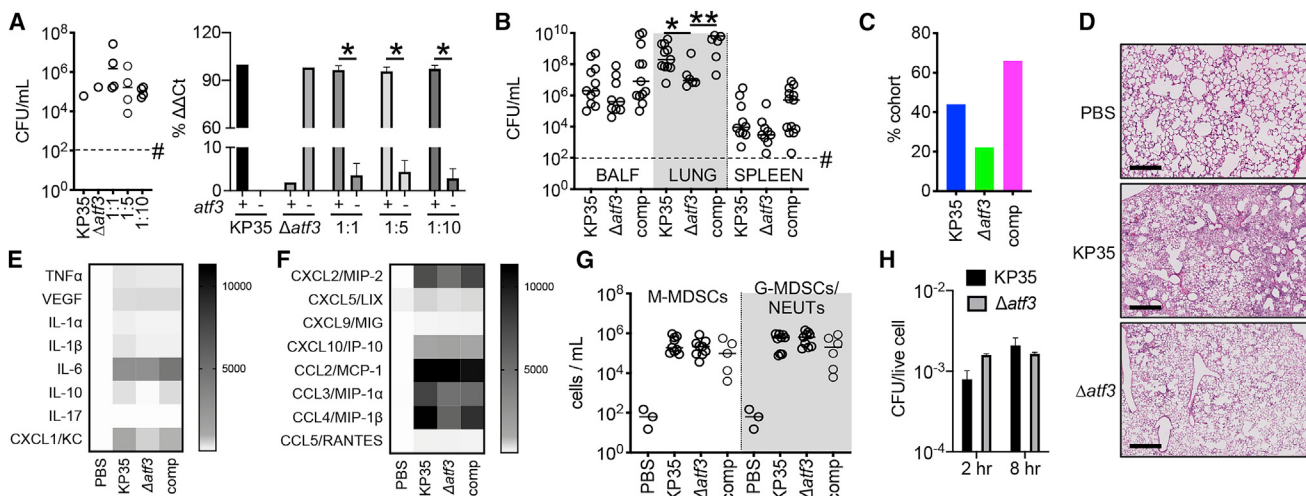


Figure 7. *atf3* promotes CRKP persistence in the lung

WT C57BL/6J mice were intranasally infected with $1-2 \times 10^8$ CFU for 48 h.

(A) In a competition experiment, mice were infected with increasing proportions of KP35: $\Delta atf3$ (1:1, 1:5, 1:10), or single isolates alone. BALF recovered and CFU enumerated by serial dilutions, and proportion of bacteria containing *atf3* (+) or lacking (-) was measured via PCR amplification with nested primers for *atf3*. n = 1 for control groups, n = 4 for experimental groups; horizontal lines are median values, and each data point represents an individual mouse; columns are mean values, with bars representing the SD.

(B) KP35, $\Delta atf3$, and $\Delta atf3$::*atf3* (comp) clearance from bronchoalveolar lavage fluid (BALF), lung homogenate, and spleen homogenate, #, the lower limit of detection. Horizontal lines represent median values, and each data point represents an individual mouse. All of the data were compiled from 3 independent experiments. n = 9–13 per condition.

(C) Percentage of the cohort at 168 h that grew bacteria from the BALF above the limit of detection (10^2 CFU/mL) (n = 3–9). For the mouse experiments, a Mann-Whitney test was performed between control and experimental conditions; *p < 0.05, **p < 0.005.

(D) Histopathology of pneumonia with KP35 and $\Delta atf3$ with PBS control in H&E-stained sections of lung. Scale bars, 500 μ m.

(E and F) Selected cytokine and chemokine content of BALF quantified by multiplex assay. The heatmap represents mean values. n = 6 per time point. (Box and whiskers presented in Figure S3.)

(G) Cellular response to infection in BALF determined by flow cytometry-monocytic myeloid-derived suppressor cells (M-MDSCs) (CD45 $^+$ CD11b $^+$ MHCII lo -Ly6C hi Ly6G lo) and granulocytic myeloid-derived suppressor cells/neutrophils (G-MDSCs/NEUT) (CD45 $^+$ CD11b $^+$ MHCII lo Ly6C hi Ly6G hi). Horizontal lines represent median values, and each data point represents an individual mouse. All of the data were compiled from 2 independent experiments. n = 3–9.

(H) A gentamicin protection assay was performed using THP-1 cells stimulated with phorbol 12-myristate 13-acetate (PMA) (1 μ M) \times 24 h. Data are presented as CFU per live cell, with columns as mean values and bars representing SEMs (n= 4).

lacking this gene. By exploiting CRISPR-Cas9 technology to generate a knockout mutant in a multi-drug-resistant clinical isolate, we confirmed that *atf3* provides a positive selective advantage for these clinically important pathogens. This acyltransferase was uniquely concentrated within one major clade of ST258 strains that have publicly available genomes, including our prototypic *K. pneumoniae* ST258 isolate KP35. Further work needs to be done to determine whether similar mechanisms of fitness are also present in clade 2 of ST258 isolates. KP35 are representative of ST258 strains from our institution (Gomez-Simmonds et al., 2015) and those that typically predominate in hospital settings worldwide (Marsh et al., 2019). KP35, along with other members of the important clade of ST258, acquired and retained the novel acyltransferase *atf3*, suggesting the importance of enhanced bacterial energetics in clinical infections.

The acquisition of *atf3* had profound effects on bacterial metabolism, particularly glucose consumption and enhanced glycolysis. KP35 had a greater expression of proteins involved in glycolysis and the TCA cycle as compared to the $\Delta atf3$ mutant. The subsequent generation of ROS and ATP by KP35 was translated into the upregulation of virtually all of the *nuo* and *nqr* genes that function in electron transport and generation of ATP. The details

of the metabolic processes upregulated in KP35 were explored by quantifying the accumulation of intracellular metabolites, also consistent with the conclusion that glycolytic and TCA cycle activity were significantly increased in the presence of *atf3*. Of note, we did not observe a relative growth defect in the $\Delta atf3$ mutant *in vitro* with either nutrient-rich media or with differing concentrations of glucose, indicating that the metabolic changes conferred by Atf3 were supplementary and did not incur a fitness cost. NQOs in *K. pneumoniae* are known to promote bacterial growth, likely due to the generation of a more favorable intracellular redox state (Zhang et al., 2018). Effects of Atf3 on growth rates *in vivo* may contribute to KP35 persistence in the lung and to the differences in the metabolites, such as glucose, that accumulate in KP35 and $\Delta atf3$ infection. However, the advantage afforded by *atf3* was most apparent in a mouse model of pneumonia. When the gene was present in only 1/10th the total infecting inoculum, bacteria expressing *atf3* significantly outcompeted the null mutant. We demonstrate that these organisms with enhanced metabolic fitness are selected and predominate within the host, even in a setting lacking antimicrobial pressure.

The annotation of *atf3* as a bacterial acyltransferase in *K. pneumoniae* did not immediately narrow the search for its

potential target(s) or explain its role in pathogenicity. There are numerous bacterial acyltransferases with diverse functions (Röttig and Steinbüchel, 2013) and >60 independent proteins identified as targets for acylation (Hentzel and Escalante-Semerena, 2015). Members of the acyltransferase superfamily 3, of which *atf3* of KP35 belongs, are present in prokaryotes and eukaryotes, with enrichment of matching orthologous sequences across *Gammaproteobacteria*, a class of bacteria to which *K. pneumoniae* belongs (Pearson et al., 2020). A notable member of this family includes OatA, an enzyme that O-acetylates the peptidoglycan of *Staphylococcus aureus*, leaving it resistant to lysozyme degradation (Bera et al., 2006; Herbert et al., 2007). This family also includes a broad range of enzymes capable of transferring acyl or acetyl groups other than aminoacyl groups, leading to a variety of post-translational modifications of integral proteins and bacterial components. In *K. pneumoniae*, one role of acyltransferases is the modification of LPS and subsequent alteration in their immunogenicity (Insua et al., 2013; Mills et al., 2017). We noted relatively minor effects of *atf3* on LPS lipid A modifications. These did not affect the immunogenicity of the organisms, as detected by cytokine induction or changes in immune cell recruitment. Other consequences of acyltransferases in *K. pneumoniae* include the acetylation of aminoglycosides (Minschew et al., 1974), capsular protein modification (Hsu et al., 2016), and toxin:antitoxin systems (Qian et al., 2018), all of which play a role in the selection of bacterial persisters.

In contrast to these many defined targets of specific bacterial acyltransferases, we found global effects of *atf3*. Post-translational modifications of prokaryotic enzymes are important mechanisms of regulating metabolism and can be achieved by the nonenzymatic donation of acetyl groups or site-specific acetylation by lysine [K] acetyltransferases (KATs) (Christensen et al., 2019b). The former is the result of accumulated acetyl-phosphate and acetyl-CoA as a consequence of glucose metabolism (Weinert et al., 2013). The latter is mediated by Nε-acetyltransferases that affect bacterial metabolism by the interaction of conserved sequences and acetyl-CoA by reversible lysine acylation (Hentzel and Escalante-Semerena, 2015). Regardless of mechanism, acetylation neutralizes the positive charge of the lysine residue and increases the size of the target enzyme, leading to decreased activity. The influence of KATs on central metabolism is conserved across taxa, is well described (Nakayasu et al., 2017), and is regulated by the energy status of the organism (Hentzel and Escalante-Semerena, 2015). Within the KP35 genome, the KATs YjaB, Riml, and PhnO with robust enzymatic activity in *E. coli* are present, but are not homologous to *atf3* (Christensen et al., 2019a). While we could not identify Atf3 of KP35 as having specific homology with known bacterial KATs, we document global post-translational consequences of Atf3 on many protein targets, especially those with metabolic activity, as would be mediated by KATs.

The acquisition of *atf3* has afforded KP35 a major metabolic advantage in the infected host. Many metabolic enzymes had both increased expression and more abundant lysine acetylation in KP35 in an *atf3*-dependent manner. Reversible lysine acylation, as we observed, generally decreases the activity of the target enzyme, and therefore is an important regulator of these processes, tempering increased transcription and activity. In

our dataset, KP35-associated acetylation of Zwf and decreased 6-gluconic acid are consistent with diminished Zwf activity, directing more glucose toward glycolysis. It remains unclear whether Zwf acetylation is a specific target of Atf3 or is one of many enzymes modified by the global increase in lysine acetylation as a consequence of increased glucose utilization, glycolysis, and acetyl group availability.

The selection and retention of an ORF like *atf3*, which provides a metabolic boost in a clinically important strain within a major ST258 clade is of both clinical and epidemiological significance. The metabolic benefit to these pathogens ascribed to the acquisition of a small acyltransferase may, in fact, be sufficient to negate the theoretical “fitness cost” associated with the maintenance of antibiotic-resistant elements. Nonetheless, we have shown that the *atf3* gene is highly relevant to the ability of these pathogens to persist *in vivo*. These studies highlight the importance of studying current clinical isolates, as even small genomic changes may have a major impact in pathogenesis and the epidemiology of infection.

STAR★METHODS

Detailed methods are provided in the online version of this paper and include the following:

- [KEY RESOURCES TABLE](#)
- [RESOURCE AVAILABILITY](#)
 - Lead contact
 - Materials availability
 - Data and code availability
- [EXPERIMENTAL MODEL AND SUBJECT DETAILS](#)
 - Animals
 - Microbe strains
 - Cell lines
- [METHOD DETAILS](#)
 - Bacterial genetics and mutagenesis
 - Baseline characteristics of bacterial isolates
 - RNA-seq and qRT-PCR
 - Cell lines
 - Mouse studies
 - Targeted metabolomics
 - Global acetylated lysine proteomics
- [QUANTIFICATION AND STATISTICAL ANALYSIS](#)
 - Statistics

SUPPLEMENTAL INFORMATION

Supplemental information can be found online at <https://doi.org/10.1016/j.celrep.2021.109196>.

ACKNOWLEDGMENTS

This work was supported by NIH K08 HL138289 (to D.A.), NIH R35 HL135800 (to A.P.), NIH R01 AI116939 (to A.-C.U.), NIH K08 AI146284 (to T.H.M.), and R01 AI123820/AI147314 (to R.K.E.). The proteomics core facility is funded by NIH P30 CA013696-45 5607 and the CCTI Flow Core by NIH S10RR027050. We thank Guoan Zhang, PhD, from the Proteomics and Metabolomics Core Facility at Weill Cornell Medicine for performing the targeted metabolomics with analysis. The graphical abstract was created with BioRender.

AUTHOR CONTRIBUTIONS

D.A. and A.P. designed the experiments, analyzed the data, and wrote the manuscript. D.A., G.B., T.H.M., M.K.A., R.K.S., T.W.F.L., V.G.C., C.E.H., S.S.S., V.C.G., and A.M.C. designed, performed, and analyzed the experiments. A.-C.U. and R.K.E. designed and analyzed the experiments.

DECLARATION OF INTERESTS

The authors declare no competing interests.

Received: November 18, 2020

Revised: February 12, 2021

Accepted: May 10, 2021

Published: June 1, 2021

REFERENCES

- Ahn, D., Peñaloza, H., Wang, Z., Wickersham, M., Parker, D., Patel, P., Koller, A., Chen, E.I., Bueno, S.M., Uhlemann, A.C., and Prince, A. (2016). Acquired resistance to innate immune clearance promotes *Klebsiella pneumoniae* ST258 pulmonary infection. *JCI Insight* 1, e89704.
- Andersson, D.I., and Hughes, D. (2010). Antibiotic resistance and its cost: is it possible to reverse resistance? *Nat. Rev. Microbiol.* 8, 260–271.
- Bachman, M.A., Breen, P., Deornellas, V., Mu, Q., Zhao, L., Wu, W., Cavalcoli, J.D., and Mobley, H.L. (2015). Genome-Wide Identification of *Klebsiella pneumoniae* Fitness Genes during Lung Infection. *MBio* 6, e00775.
- Bera, A., Biswas, R., Herbert, S., and Götz, F. (2006). The presence of peptidoglycan O-acetyltransferase in various staphylococcal species correlates with lysozyme resistance and pathogenicity. *Infect. Immun.* 74, 4598–4604.
- Blin, C., Passet, V., Touchon, M., Rocha, E.P.C., and Brisse, S. (2017). Metabolic diversity of the emerging pathogenic lineages of *Klebsiella pneumoniae*. *Environ. Microbiol.* 19, 1881–1898.
- Borer, A., Saidel-Odes, L., Riesenbergs, K., Eskira, S., Peled, N., Nativ, R., Schlaeffer, F., and Sherf, M. (2009). Attributable mortality rate for carbapenem-resistant *Klebsiella pneumoniae* bacteremia. *Infect. Control Hosp. Epidemiol.* 30, 972–976.
- Bruchmann, S., Feltwell, T., Parkhill, J., and Short, F.L. (2021). Identifying virulence determinants of multidrug-resistant *Klebsiella pneumoniae* in *Galleria mellonella*. *Pathog. Dis.* 79, ftab009.
- Caboni, M., Pédrón, T., Rossi, O., Goulding, D., Pickard, D., Citiulo, F., MacLennan, C.A., Dougan, G., Thomson, N.R., Saul, A., et al. (2015). An O antigen capsule modulates bacterial pathogenesis in *Shigella sonnei*. *PLoS Pathog.* 11, e1004749.
- Callura, J.M., Cantor, C.R., and Collins, J.J. (2012). Genetic switchboard for synthetic biology applications. *Proc. Natl. Acad. Sci. USA* 109, 5850–5855.
- Christensen, D.G., Baumgartner, J.T., Xie, X., Jew, K.M., Basisty, N., Schilling, B., Kuhn, M.L., and Wolfe, A.J. (2019a). Mechanisms, Detection, and Relevance of Protein Acetylation in Prokaryotes. *MBio* 10, e02708-18.
- Christensen, D.G., Xie, X., Basisty, N., Byrnes, J., McSweeney, S., Schilling, B., and Wolfe, A.J. (2019b). Post-translational Protein Acetylation: An Elegant Mechanism for Bacteria to Dynamically Regulate Metabolic Functions. *Front. Microbiol.* 10, 1604.
- Cillóniz, C., Domínguez, C., and Torres, A. (2019). An overview of guidelines for the management of hospital-acquired and ventilator-associated pneumonia caused by multidrug-resistant Gram-negative bacteria. *Curr. Opin. Infect. Dis.* 32, 656–662.
- Clinical and Laboratory Standards Institute (2017). M100. Performance Standards for Antimicrobial Susceptibility Testing, 27th ed. (Clinical and Laboratory Standards Institute).
- Creecy, J.P., and Conway, T. (2015). Quantitative bacterial transcriptomics with RNA-seq. *Curr. Opin. Microbiol.* 23, 133–140.
- Davis, M.R., Jr., and Goldberg, J.B. (2012). Purification and visualization of lipopolysaccharide from Gram-negative bacteria by hot aqueous-phenol extraction. *J. Vis. Exp.* 63, 3916.
- Dibrov, P., Dibrov, E., and Pierce, G.N. (2017). Na+-NQR (Na+-translocating NADH:ubiquinone oxidoreductase) as a novel target for antibiotics. *FEMS Microbiol. Rev.* 41, 653–671.
- Dimroth, P. (1987). Sodium ion transport decarboxylases and other aspects of sodium ion cycling in bacteria. *Microbiol. Rev.* 51, 320–340.
- Doi, Y., Bonomo, R.A., Hooper, D.C., Kaye, K.S., Johnson, J.R., Clancy, C.J., Thaden, J.T., Stryjewski, M.E., and van Duin, D.; Gram-Negative Committee of the Antibacterial Resistance Leadership Group (ARLG) (2017). Gram-Negative Bacterial Infections: Research Priorities, Accomplishments, and Future Directions of the Antibacterial Resistance Leadership Group. *Clin. Infect. Dis.* 64 (Suppl_1), S30–S35.
- Doucette, C.D., Schwab, D.J., Wingreen, N.S., and Rabinowitz, J.D. (2011). -Ketoglutarate coordinates carbon and nitrogen utilization via enzyme I inhibition. *Nat. Chem. Biol.* 7, 894–901.
- El Hamidi, A., Tirsoaga, A., Novikov, A., Hussein, A., and Caroff, M. (2005). Microextraction of bacterial lipid A: easy and rapid method for mass spectrometric characterization. *J. Lipid Res.* 46, 1773–1778.
- Erhardt, H., Steimle, S., Muders, V., Pohl, T., Walter, J., and Friedrich, T. (2012). Disruption of individual nuo-genes leads to the formation of partially assembled NADH:ubiquinone oxidoreductase (complex I) in *Escherichia coli*. *Biochim. Biophys. Acta* 1817, 863–871.
- Ernst, C.M., Braxton, J.R., Rodriguez-Osorio, C.A., Zagleboyo, A.P., Li, L., Pironti, A., Manson, A.L., Nair, A.V., Benson, M., Cummins, K., et al. (2020). Adaptive evolution of virulence and persistence in carbapenem-resistant *Klebsiella pneumoniae*. *Nat. Med.* 26, 705–711.
- Giddins, M.J., Macesic, N., Annavajhala, M.K., Stump, S., Khan, S., McConville, T.H., Mehta, M., Gomez-Simmonds, A., and Uhlemann, A.C. (2018). Successive Emergence of Ceftazidime-Avibactam Resistance through Distinct Genomic Adaptations in bla_{KPC-2}-Harboring *Klebsiella pneumoniae* Sequence Type 307 Isolates. *Antimicrob. Agents Chemother.* 62, e02101-17.
- Gomez-Simmonds, A., and Uhlemann, A.C. (2017). Clinical Implications of Genomic Adaptation and Evolution of Carbapenem-Resistant *Klebsiella pneumoniae*. *J. Infect. Dis.* 215 (Suppl_1), S18–S27.
- Gomez-Simmonds, A., Greenman, M., Sullivan, S.B., Tanner, J.P., Sowash, M.G., Whittier, S., and Uhlemann, A.C. (2015). Population Structure of *Klebsiella pneumoniae* Causing Bloodstream Infections at a New York City Tertiary Care Hospital: Diversification of Multidrug-Resistant Isolates. *J. Clin. Microbiol.* 53, 2060–2067.
- Gomez-Simmonds, A., Annavajhala, M.K., McConville, T.H., Dietz, D.E., Shoucri, S.M., Laracy, J.C., Rozenberg, F.D., Nelson, B., Greendyke, W.G., Furuya, E.Y., et al. (2020). Carbapenemase-producing Enterobacteriales causing secondary infections during the COVID-19 crisis at a New York City hospital. *J. Antimicrob. Chemother.* 76, 380–384.
- Haas, B.J., Chin, M., Nusbaum, C., Birren, B.W., and Livny, J. (2012). How deep is deep enough for RNA-Seq profiling of bacterial transcriptomes? *BMC Genomics* 13, 734.
- Haug, K., Cochrane, K., Nainala, V.C., Williams, M., Chang, J., Jayaseelan, K.V., and O'Donovan, C. (2020). MetaboLights: a resource evolving in response to the needs of its scientific community. *Nucleic Acids Res.* 48 (D1), D440–D444.
- Hentzel, K.L., and Escalante-Semerena, J.C. (2015). Acylation of Biomolecules in Prokaryotes: a Widespread Strategy for the Control of Biological Function and Metabolic Stress. *Microbiol. Mol. Biol. Rev.* 79, 321–346.
- Herbert, S., Bera, A., Nerz, C., Kraus, D., Peschel, A., Goerke, C., Meehl, M., Cheung, A., and Götz, F. (2007). Molecular basis of resistance to muramidase and cationic antimicrobial peptide activity of lysozyme in staphylococci. *PLoS Pathog.* 3, e102.
- Hsu, C.R., Liao, C.H., Lin, T.L., Yang, H.R., Yang, F.L., Hsieh, P.F., Wu, S.H., and Wang, J.T. (2016). Identification of a capsular variant and characterization of capsular acetylation in *Klebsiella pneumoniae* PLA-associated type K57. *Sci. Rep.* 6, 31946.

- Inouye, M., Dashnow, H., Raven, L.A., Schultz, M.B., Pope, B.J., Tomita, T., Zobel, J., and Holt, K.E. (2014). SRST2: rapid genomic surveillance for public health and hospital microbiology labs. *Genome Med.* 6, 90.
- Insua, J.L., Llobet, E., Moranta, D., Pérez-Gutiérrez, C., Tomás, A., Garmendia, J., and Bengoechea, J.A. (2013). Modeling *Klebsiella pneumoniae* pathogenesis by infection of the wax moth *Galleria mellonella*. *Infect. Immun.* 81, 3552–3565.
- Jiang, Y., Chen, B., Duan, C., Sun, B., Yang, J., and Yang, S. (2015). Multigene editing in the *Escherichia coli* genome via the CRISPR-Cas9 system. *Appl. Environ. Microbiol.* 81, 2506–2514.
- Jiang, X., Bomgarden, R., Brown, J., Drew, D.L., Robitaille, A.M., Viner, R., and Huhmer, A.R. (2017). Sensitive and Accurate Quantitation of Phosphopeptides Using TMT Isobaric Labeling Technique. *J. Proteome Res.* 16, 4244–4252.
- Kohler, P.P., Volling, C., Green, K., Uleryk, E.M., Shah, P.S., and McGeer, A. (2017). Carbapenem Resistance, Initial Antibiotic Therapy, and Mortality in *Klebsiella pneumoniae* Bacteremia: A Systematic Review and Meta-Analysis. *Infect. Control Hosp. Epidemiol.* 38, 1319–1328.
- Langmead, B., and Salzberg, S.L. (2012). Fast gapped-read alignment with Bowtie 2. *Nat. Methods* 9, 357–359.
- Letunic, I., and Bork, P. (2019). Interactive Tree Of Life (iTOL) v4: recent updates and new developments. *Nucleic Acids Res.* 47 (W1), W256–W259.
- Liu, Y.Y., Chandler, C.E., Leung, L.M., McElheny, C.L., Mettus, R.T., Shanks, R.M.Q., Liu, J.H., Goodlett, D.R., Ernst, R.K., and Doi, Y. (2017). Structural Modification of Lipopolysaccharide Conferred by *mcr-1* in Gram-Negative ES-KAPE Pathogens. *Antimicrob. Agents Chemother.* 61, e00580-17.
- Love, M.I., Huber, W., and Anders, S. (2014). Moderated estimation of fold change and dispersion for RNA-seq data with DESeq2. *Genome Biol.* 15, 550.
- Marsh, J.W., Mustapha, M.M., Griffith, M.P., Evans, D.R., Ezeonwuka, C., Pasculle, A.W., Shutt, K.A., Sundermann, A., Ayres, A.M., Shields, R.K., et al. (2019). Evolution of Outbreak-Causing Carbapenem-Resistant *Klebsiella pneumoniae* ST258 at a Tertiary Care Hospital over 8 Years. *MBio* 10, e01945-19.
- McConville, T.H., Annavajhala, M.K., Giddins, M.J., Macesic, N., Herrera, C.M., Rozenberg, F.D., Bhushan, G.L., Ahn, D., Mancia, F., Trent, M.S., and Uhlemann, A.C. (2020). CrrB Positively Regulates High-Level Polymyxin Resistance and Virulence in *Klebsiella pneumoniae*. *Cell Rep.* 33, 108313.
- McConville, T.H., Giddins, M.J., and Uhlemann, A.C. (2021). An efficient and versatile CRISPR-Cas9 system for genetic manipulation of multi-drug resistant *Klebsiella pneumoniae*. *STAR Protoc* 2, 100373.
- Mills, G., Dumigan, A., Kidd, T., Hobley, L., and Bengoechea, J.A. (2017). Identification and Characterization of Two *Klebsiella pneumoniae* *lpxL* Lipid A Late Acyltransferases and Their Role in Virulence. *Infect. Immun.* 85, e00068-17.
- Minshew, B.H., Holmes, R.K., Sanford, J.P., and Baxter, C.R. (1974). Transferable resistance to tobramycin in *Klebsiella pneumoniae* and *Enterobacter cloacae* associated with enzymatic acetylation of tobramycin. *Antimicrob. Agents Chemother.* 6, 492–497.
- Nakayasu, E.S., Burnet, M.C., Walukiewicz, H.E., Wilkins, C.S., Shukla, A.K., Brooks, S., Plutz, M.J., Lee, B.D., Schilling, B., Wolfe, A.J., et al. (2017). Ancient Regulatory Role of Lysine Acetylation in Central Metabolism. *MBio* 8, e01894-17.
- Navarrete-Perea, J., Yu, Q., Gygi, S.P., and Paulo, J.A. (2018). Streamlined Tandem Mass Tag (SL-TMT) Protocol: An Efficient Strategy for Quantitative (Phospho)proteome Profiling Using Tandem Mass Tag-Synchronous Precursor Selection-MS3. *J. Proteome Res.* 17, 2226–2236.
- Paczosa, M.K., Silver, R.J., McCabe, A.L., Tai, A.K., McLeish, C.H., Lazinski, D.W., and Mecsas, J. (2020). Transposon Mutagenesis Screen of *Klebsiella pneumoniae* Identifies Multiple Genes Important for Resisting Antimicrobial Activities of Neutrophils in Mice. *Infect. Immun.* 88, e00034-20.
- Pan, Y.J., Lin, T.L., Chen, C.T., Chen, Y.Y., Hsieh, P.F., Hsu, C.R., Wu, M.C., and Wang, J.T. (2015). Genetic analysis of capsular polysaccharide synthesis gene clusters in 79 capsular types of *Klebsiella* spp. *Sci. Rep.* 5, 15573.
- Pearson, C.R., Tindall, S.N., Herman, R., Jenkins, H.T., Bateman, A., Thomas, G.H., Potts, J.R., and Van der Woude, M.W. (2020). Acetylation of Surface Carbohydrates in Bacterial Pathogens Requires Coordinated Action of a Two-Domain Membrane-Bound Acyltransferase. *MBio* 11. <https://doi.org/10.1128/mBio.01364-20>.
- Peñaloza, H.F., Noguera, L.P., Ahn, D., Vallejos, O.P., Castellanos, R.M., Vazquez, Y., Salazar-Echegarai, F.J., González, L., Suazo, I., Pardo-Roa, C., et al. (2019). Interleukin-10 Produced by Myeloid-Derived Suppressor Cells Provides Protection to Carbapenem-Resistant *Klebsiella pneumoniae* Sequence Type 258 by Enhancing Its Clearance in the Airways. *Infect. Immun.* 87, e00665-18.
- Pitout, J.D., Nordmann, P., and Poirel, L. (2015). Carbapenemase-Producing *Klebsiella pneumoniae*, a Key Pathogen Set for Global Nosocomial Dominance. *Antimicrob. Agents Chemother.* 59, 5873–5884.
- Poe, S.L., Arora, M., Oriss, T.B., Yarlagadda, M., Isse, K., Khare, A., Levy, D.E., Lee, J.S., Mallampalli, R.K., Chan, Y.R., et al. (2013). STAT1-regulated lung MDSC-like cells produce IL-10 and efferocytose apoptotic neutrophils with relevance in resolution of bacterial pneumonia. *Mucosal Immunol.* 6, 189–199.
- Qian, H., Yao, Q., Tai, C., Deng, Z., Gan, J., and Ou, H.Y. (2018). Identification and characterization of acetyltransferase-type toxin-antitoxin locus in *Klebsiella pneumoniae*. *Mol. Microbiol.* 108, 336–349.
- Röttig, A., and Steinbüchel, A. (2013). Acyltransferases in bacteria. *Microbiol. Mol. Biol. Rev.* 77, 277–321.
- Satlin, M.J., Chen, L., Patel, G., Gomez-Simmonds, A., Weston, G., Kim, A.C., Seo, S.K., Rosenthal, M.E., Sperber, S.J., Jenkins, S.G., et al. (2017). Multi-center Clinical and Molecular Epidemiological Analysis of Bacteremia Due to Carbapenem-Resistant *Enterobacteriaceae* (CRE) in the CRE Epicenter of the United States. *Antimicrob. Agents Chemother.* 61, e02349-16.
- Stamatakis, A. (2014). RAxML version 8: a tool for phylogenetic analysis and post-analysis of large phylogenies. *Bioinformatics* 30, 1312–1313.
- Tzouvelekis, L.S., Miriagou, V., Kotsakis, S.D., Spyridopoulou, K., Athanasiou, E., Karagianni, E., Tzelepi, E., and Daikos, G.L. (2013). KPC-producing, multi-drug-resistant *Klebsiella pneumoniae* sequence type 258 as a typical opportunistic pathogen. *Antimicrob. Agents Chemother.* 57, 5144–5146.
- van Duin, D., Arias, C.A., Komarow, L., Chen, L., Hanson, B.M., Weston, G., Cober, E., Garner, O.B., Jacob, J.T., Satlin, M.J., et al.; Multi-Drug Resistant Organism Network Investigators (2020). Molecular and clinical epidemiology of carbapenem-resistant Enterobacteriales in the USA (CRACKLE-2): a prospective cohort study. *Lancet Infect. Dis.* 20, 731–741.
- Vornhagen, J., Sun, Y., Breen, P., Forsyth, V., Zhao, L., Mobley, H.L.T., and Bachman, M.A. (2019). The *Klebsiella pneumoniae* citrate synthase gene, gltA, influences site specific fitness during infection. *PLoS Pathog.* 15, e1008010.
- Weinert, B.T., Iesmantavicius, V., Wagner, S.A., Schölz, C., Gummesson, B., Beli, P., Nyström, T., and Choudhary, C. (2013). Acetyl-phosphate is a critical determinant of lysine acetylation in *E. coli*. *Mol. Cell* 51, 265–272.
- Wong, J.L.C., Romano, M., Kerry, L.E., Kwong, H.S., Low, W.W., Brett, S.J., Clements, A., Beis, K., and Frankel, G. (2019). OmpK36-mediated Carbapenem resistance attenuates ST258 *Klebsiella pneumoniae* in vivo. *Nat. Commun.* 10, 3957.
- Xiong, H., Carter, R.A., Leiner, I.M., Tang, Y.W., Chen, L., Kreiswirth, B.N., and Pamer, E.G. (2015). Distinct Contributions of Neutrophils and CCR2+ Monocytes to Pulmonary Clearance of Different *Klebsiella pneumoniae* Strains. *Infect. Immun.* 83, 3418–3427.
- Xu, L., Sun, X., and Ma, X. (2017). Systematic review and meta-analysis of mortality of patients infected with carbapenem-resistant *Klebsiella pneumoniae*. *Ann. Clin. Microbiol. Antimicrob.* 16, 18.
- Zhang, L., Bao, W., Wei, R., Fu, S., and Gong, H. (2018). Inactivating NADH:quinone oxidoreductases affects the growth and metabolism of *Klebsiella pneumoniae*. *Biotechnol. Appl. Biochem.* 65, 857–864.

STAR★METHODS

KEY RESOURCES TABLE

REAGENT or RESOURCE	SOURCE	IDENTIFIER
Antibodies		
PerCP-Cy5.5-labeled anti-CD11c	Biolegend	Cat# 117328; Monoclonal; Clone N418; RRID: AB_2129641
PE-Cy7-labeled anti-F4/80	Biolegend	Cat# 123113; Monoclonal; Clone BM8; RRID: AB_893490
Phycoerythrin (PE)-CF594-labeled anti-Ly6C	BD Biosciences	Cat# 562728; Monoclonal; Clone AL-21; RRID: AB_2737749
BV510-labeled anti-CD11b	Biolegend	Cat# 101263; Monoclonal; Clone M1/70; RRID: AB_2629529
BV605-labeled anti-Ly6G	BD Biosciences	Cat# 563005; Monoclonal; Clone 1A8 RRID: AB_2737946
APC-Cy7-labeled anti-MHCII	Biolegend	Cat# 107628; Monoclonal; Clone M5/114.15.2; RRID: AB_2069377
AF700-labeled anti-CD45	Biolegend	Cat# 103128; Monoclonal; Clone 30-F11; RRID: AB_493715;
AF647-labeled anti-Siglec F	BD Biosciences	Cat# 562680; Monoclonal; Clone E50-2440; RRID: AB_2687570
Fc block (anti-mouse CD16/32)	Biolegend	Cat# 101302; Monoclonal; Clone 93; RRID: AB_312801
Bacterial and virus strains		
pUC19 DNA	Thermo Scientific	Cat# SD0061
pCas	Jiang et al., 2015	Cat# 62225; Addgene_62225
pUC19_CRISPR_Datf3	This study	N/A
pcr2.1_topo_Atf3 (complementation plasmid)	This study	N/A
Chemicals, peptides, and recombinant proteins		
Zeocin	Invivogen	Cat# ant-zn-05
L-(+)-arabinose	Sigma-Aldrich	Cat# A3256; CAS# 5328-37-0
Penicillin-streptomycin	Corning	Cat# 30-002-Cl; Lot# 30002307
Isobutyric acid	Sigma-Aldrich	Cat# I1754; CAS# 79-31-2
Ammonium hydroxide	Sigma-Aldrich	Cat# 221228; CAS# 1336-21-6

(Continued on next page)

Continued

REAGENT or RESOURCE	SOURCE	IDENTIFIER
Norharmane	Sigma-Aldrich	Cat# N6252; CAS# 244-63-3
Chloroform	Sigma-Aldrich	Cat# C606SK-4; CAS# 67-66-3
Methanol	Sigma-Aldrich	Cat# A456-1; CAS# 67-56-1
TRIzol reagent	Invitrogen	Cat# 15596026; Lot# 42902
Hydrogen peroxide solution 30% (w/w)	Sigma-Aldrich	Cat# H1009; CAS# 7722-84-1; Lot# MKBZ7948V
Lysozyme	Sigma-Aldrich	Cat# L6876; Lot# SLCC4285
D-(+)-glucose	Sigma-Aldrich	Cat# G7021; CAS# 50-99-7; Lot# SLBZ6903
Sodium pyruvate	Sigma-Aldrich	Cat# P5280; CAS# 113-24-6; Lot# SLBP4879V
α -ketoglutaric acid	Sigma-Aldrich	Cat# 75890; CAS# 328-50-7
Disodium succinate	Sigma-Aldrich	Cat# W327700; CAS# 150-90-3; Lot# MKCC2485
Protocol crystal violet	Fisher Scientific	Cat# 255-960B
Phorbol 12-myristate 13-acetate (PMA)	Sigma-Aldrich	Cat# P8139; CAS# 16561-29-8
Gentamicin	Sigma-Aldrich	Cat# G1397; CAS# 1405-41-0
Saponin	Sigma-Aldrich	Cat# S4521; CAS# 8047-15-2; Lot# 121K7004
Formalin free tissue fixative	Sigma-Aldrich	Cat# A5472; Lot# SLBV4022
Methanol, ultrapure, HPLC grade, 99.8+%	Alfa Aesar	Cat# 22909; Lot# Q17D708
EPPS	Sigma-Aldrich	Cat# E9502; CAS# 16052-06-5; Lot# SLCB4421
Bicinchoninic acid (BCA)	Thermo Scientific	Cat# 23225; Lot# VB297450
Dithiothreitol (DTT)	Sigma-Aldrich	Cat# D0632; CAS# 3483-12-3; Lot# SLBW1508
Tris(2-carboxyethyl)phosphine) (TCEP)	Sigma-Aldrich	Cat# C4706; CAS# 51805-45-9; Lot# SLCB2139
Iodoacetamide (IAA)	Sigma-Aldrich	Cat# I1149; CAS# 144-48-9; Lot# SLCC6164
Lys-C	Wako (Fujifilm)	Cat# 125-05061; Lot# SKM6660
Trypsin	Promega	Cat# V5111; Lot# 0000459830

(Continued on next page)

Continued

REAGENT or RESOURCE	SOURCE	IDENTIFIER
Trifluoroacetic acid (TFA)	Thermo Scientific	Cat# 28904; CAS# 76-05-1; Lot# VH312275
Critical commercial assays		
Pro-Q emerald 300 lipopolysaccharide gel stain kit	Invitrogen	Cat# P20495
PM1 phenotype microarray	Biolog	Cat# 12111; Lot# 3410131
Seahorse XF24 cell culture microplates	Agilent	Cat# 100777-004; Lot# 21720
Seahorse XF glycolysis stress test kit	Agilent	Cat# 103020-100; Lot# 17019693
MitoSox	Invitrogen	Cat# M36008
BacTiter-glo microbial cell viability assay	Promega	Cat# G8230
E.Z.N.A. Total RNA Kit I	Omega Bio-tek	Cat# R6834-02; Lot# R68345371-10
DNA-free DNA removal kit	Invitrogen	Cat# AM1906
MICROBExpress	Ambion, Life Technologies	Cat# AM1905
Truseq stranded mRNA library prep	Illumina	Cat# 20020594
High-capacity cDNA reverse transcription kit	Applied Biosystems	Cat# 4368814
PowerSYBR green PCR master mix	Applied Biosystems	Cat# 4368708
Mouse cytokine array / chemokine array 31-plex	Eve Technologies	Cat# MD31
DNeasy blood and tissue kit	QIAGEN	Cat# 69504
LIVE/DEAD fixable blue dead cell stain kit, for UV excitation	Molecular Probes	Cat# L23105
Glucose assay kit	Abcam	Cat# ab65333
Uniform dye microspheres	Bang Laboratories	Cat# FSO7F; Lot# 12980
10-plex TMT kit	Thermo Scientific	Cat# 90111; Lot# UB279981
PTMScan® acetyl-lysine motif [Ac-K]	Cell Signaling	Cat# 13416
Microscan	Beckman Coulter	Cat# NM42
Deposited data		
Full bacterial genome sequencing and bacterial RNA-seq (KP35)	NCBI Short Read Archive (SRA)	NCBI: SAMN18588135
Full bacterial genome sequencing and bacterial RNA-seq (KP35::Δatf3)	NCBI Short Read Archive (SRA)	NCBI: SAMN18588136
Acetylome (KP35, KP35::Δatf3)	MassIVE, University of California, San Diego	https://massive.ucsd.edu/ProteoSAFe/static/massive.jsp MassIVE: MSV000087181
Bacterial and BALF metabolomics	Metabolights (Haug et al., 2020)	https://www.ebi.ac.uk/metabolights/ MetaboLights: MTBLS2640
Experimental models: cell lines		
Human monocytes (THP-1 s)	ATCC	TIB-202
Experimental models: organisms/strains		
Mouse: C57BL/6J	The Jackson Laboratories	JAX: 000664
<i>Klebsiella pneumoniae</i> , clinical isolate 35	Ahn et al., 2016	N/A
Isogenic mutant – KP35::Δatf3	This study	N/A
Complemented mutant – KP35::Δatf3::Δatf3	This study	N/A
<i>Klebsiella pneumoniae</i> , KPPR1	ATCC	Cat# 43816
<i>Pseudomonas aeruginosa</i> (PAO1)	Our laboratory	N/A

(Continued on next page)

Continued

REAGENT or RESOURCE	SOURCE	IDENTIFIER
Oligonucleotides		
Primers for the competition experiment – <i>atf3</i>	This study	N/A
Present FWD (ATG TGG GTG GAT TAT GCT AAG G)		
<i>atf3</i> Absent FWD (ATG AGT CTA GAA TGT TAT A)	This study	N/A
<i>atf3</i> Common REV (GGC ATA TGG AAT GAA TAT ATA A)	This study	N/A
Primers for NADH:ubiquinone oxidoreductases: see Table S1	This study	N/A
Software and algorithms		
SRST2	Inouye et al., 2014	https://github.com/katholt/srst2
Snippy		https://github.com/tseemann/snippy
RAxML	Stamatakis, 2014	https://github.com/stamatak/standard-RAxML
iTOL	Letunic and Bork, 2019	https://github.com/iBioLyfe/iTOL
Geneious	Biomatters	https://www.geneious.com
Bowtie2	Langmead and Salzberg, 2012	http://bowtie-bio.sourceforge.net/bowtie2/index.shtml
DESeq2	Love et al., 2014	https://github.com/mikelove/DESeq2
Trimmomatic		https://github.com/timflutre/trimmomatic
KEGG pathway analysis, KEGG Mapper	Kanehisa Laboratories	https://www.genome.jp/kegg/
MetaboAnalyst	McGill	https://www.metaboanalyst.ca/
FlexAnalysis software	Bruker Daltonics	https://www.bruker.com/en.html ; v4.30
FlowJo X software	TreeStart Inc.	https://www.flowjo.com ; ver 10.0.8
Graph pad prism	Version 8.4.0 (455), February 20, 2020	https://www.graphpad.com
ImageJ	National Institutes of Health	https://imagej.nih.gov/ij ; Java 1.8.0_172
Endnote X9	Endnote X9.3.2 (Bld 15235)	endnote.com
StepOne Software	Applied Biosystems	Ver 2.2.2
MaxQuant	Max Plank Institute of Biochemistry	https://www.maxquant.org/download_asset/maxquant/latestv1.6.17.0
Other		
Novex 16% tricine gel	Invitrogen	Cat# EC6695BOX; Lot# 19100940
M9 minimal salts (2X)	GIBCO	Cat# A13744-01; Lot# 2121257
RPMI 1640, 1x with L-glutamine	Corning	Cat# 10-040-CV; Lot# 33720004
Fetal bovine serum	GIBCO	Cat# 26140-079
XF base medium minimal DMEM	Agilent	Cat# 102353-100; Lot# 17619002
Difco LB broth, mill (Luria-Bertani) (LB) media	BD	Cat# 244610; Lot# 9324045
BBL trypticase soy broth (TS) media	BD	Cat# 211768; Lot# 1300142
TrypLE express	GIBCO	Cat# 12604021; Lot# 2085370

RESOURCE AVAILABILITY**Lead contact**

Further information and requests for resources and reagents should be directed to and will be fulfilled by the lead contact, Danielle Ahn (dsa2120@cumc.columbia.edu).

Materials availability

A standard CRISPR plasmid (pCAS) was used to generate KP35:: $\Delta atf3$ is available at addgene; catalog #62225. <https://www.addgene.org/62225/>. The gene specific plasmid (pUC19_CRISPR_Datf3) and complementation plasmid (pcr2.1_topo_At3) are available without restriction upon request.

Data and code availability

The RNA-seq datasets and full genome sequencing of KP35 and the $\Delta atf3$ isogenic mutant generated during this study are available in the NCBI Short Read Archive (SRA) and are assigned a BioProject ID: PRJNA719112, [NCBI SRA: SAMN18588135](#) (KP35), and [NCBI SRA: SAMN18588136](#) (KP35:: $\Delta atf3$)

The acetylomes of KP35 and the $\Delta atf3$ isogenic mutant are available through MassIVE (available through <https://massive.ucsd.edu/ProteoSAFe/static/massive.jsp>, MassIVE: [MSV000087181](#) and the metabolomics data are available through Metabolights (available through <https://www.ebi.ac.uk/>, MetaboLights: [MTBLS2640](#)).

EXPERIMENTAL MODEL AND SUBJECT DETAILS**Animals**

In vivo experiments were performed using 8-week-old, male C57BL/6J mice (Jackson Laboratories, Stock No. 000664). Sample sizes were predetermined by power calculations using a 1 log reduction in bacterial burden in the BALF of infected mice. No mice were excluded and were placed into control or infection groups at random. Treatment groups were not blinded. Experimental mice were weighed daily and given a body conditioning score. Since the mice were noted to be bright, alert and active with 20% weight loss ([Ahn et al., 2016](#)), after careful review by the veterinarians and IACUC, the animals were allowed to lose 30% of their initial body weight as long as their body conditioning score remained high. All animal experiments were performed in accordance with the guidelines of the IACUC at Columbia University (protocol number AAAS4464).

Microbe strains

We selected a representative *K. pneumoniae* ST258 clinical isolate 35 (KP35) from a patient with bacteremia which was comprehensively studied in previous publications ([Ahn et al., 2016](#); [Gomez-Simmonds and Uhlemann, 2017](#)). *Pseudomonas aeruginosa* strain PAO1 and *K. pneumoniae* KPPR1 (ATCC 43816) were used as controls. All assays were performed on bacteria grown overnight, subcultured to logarithmic phase and normalized to OD₆₀₀ of 0.5.

Cell lines**Human monocytes (THP-1 s)**

ATCC TIB-202: monocytes from a human male with acute monocytic leukemia. THP-1 cells were grown at 37°C with 5% CO₂ in RPMI 1640 with L-glutamine cell culture medium with 10% heat-inactivated fetal bovine serum. THP-1 s were activated with 1 μM phorbol 12-myristate 13-acetate (PMA) for 24 hours prior to infection and subsequently weaned to antibiotic free media 24 hours prior to testing.

METHOD DETAILS**Bacterial genetics and mutagenesis****Screening for *atf3* presence**

To determine the prevalence of *atf3* in *K. pneumoniae*, 218 publicly available genome assemblies were downloaded from NCBI. SRST2 ([Inouye et al., 2014](#)) was used for MLST typing and to identify isolates belonging to sequence type 258 (ST258). A custom SRST2 gene database was then made with the *atf3* gene sequence from the KP35 reference genome and used to determine the presence or absence of the *atf3* gene in each genomic assembly.

Phylogenetic analyses

To reconstruct the phylogenetic relationships between all public *K. pneumoniae* genomes, and within *K. pneumoniae* ST258, we used Snippy to identify core genome single nucleotide polymorphisms (SNPs) by mapping each genome against the ST258 KPNIH1 reference genome (GenBank CP008827.1). A maximum-likelihood phylogeny was then created with RAxML ([Stamatakis, 2014](#)) with 100 bootstrap replicates based on concatenated core genome SNPs. Phylogenetic trees were visualized and annotated in iTOL ([Letunic and Bork, 2019](#)).

Gene editing using CRISPR-Cas9

To allow for efficient genetic manipulation in multi-drug resistant *K. pneumoniae*, we utilized our recently optimized single plasmid CRISPR-Cas9 / lambda red recombineering system ([Jiang et al., 2015](#); [McConville et al., 2020](#); [McConville et al., 2021](#)). For the gene deletion, we first analyzed the wild-type *atf3* sequence via the CRISPRdirect website to identify an appropriate N20 sequence, which was incorporated into an *atf3* sgRNA. To knockout *atf3*, the homology was engineered to contain a 122 bp deletion surrounding the cas9 cut site. The *atf3* specific sgRNA and homology cassettes were cloned into the pUC19_CRISPR vector (pUC19_CRISPR_Datf3). The sequence confirmed plasmid was inserted into the clinical isolate KP35 via electroporation and

appropriate transformants were identified through colony PCR. Transformants were grown at 30°C under Zeocin selection and induced with 2% L-(+)-arabinose after 2 hours. Following 6+ hours of induction the cultures were diluted 1:100 and plated on low salt LB with Zeocin and L-(+)-arabinose. Appropriate mutants were identified with colony PCR and sanger sequencing (Genewiz). Mutants were cured of the CRISPR plasmid with serial passage on non-selective media. To ensure no off-target editing occurred, we performed whole genome sequencing (WGS) with hybrid assembly utilizing Illumina and Nanopore reads (Giddins et al., 2018). The complemented isolate was constructed using a high copy number plasmid containing the *atf3* gene with a Zeocin resistant cassette (pcr2.1_topo_Atf3).

Baseline characteristics of bacterial isolates

LPS studies

Lipid A analysis

K. pneumoniae strains were cultured for 18 hr at 37°C with shaking in 5 mL Luria-Bertani (LB). Lipid A was extracted from cell pellets using an ammonium hydroxide-isobutyric acid-based procedure (El Hamidi et al., 2005; Liu et al., 2017). Briefly, approximately 5 mL of cell culture was pelleted and resuspended in 400 µL of 70% isobutyric acid and 1 M ammonium hydroxide (5:3 [vol/vol]). Samples were incubated for 1 h at 100°C and centrifuged at 2,000 × g for 15 min. Supernatants were collected, added to endotoxin-free water (1:1 [vol/vol]), snap-frozen on dry ice, and lyophilized overnight. The resultant material was washed twice with 1 mL methanol, and lipid A was extracted using 80 µL of a mixture of chloroform, methanol, and water (3:1:0.25 [vol/vol/vol]). Once extracted, 1 µL of the concentrate was spotted on a steel re-usable MALDI plate followed by 1 µL of 10 mg/ml norharmane matrix in chloroform-methanol (2:1 [vol/vol]) and then was air-dried. All samples were analyzed on a Bruker Microflex mass spectrometer (Bruker Daltonics, Billerica, MA) in the negative-ion mode with reflectron mode. An electrospray tuning mix (Agilent, Palo Alto, CA) was used for mass calibration. Spectral data were analyzed with FlexAnalysis software. The resulting spectra were used to estimate the lipid A structures present in each strain based on their predicted structures and molecular weights.

O-antigen analysis

To visualize the O-antigen ladder of bacteria, LPS was first isolated using a hot phenol extraction (Davis and Goldberg, 2012) from overnight cultures normalized to OD₆₀₀ of 0.5 after 1:10 dilution. Samples were treated with DNase and RNase for 30 min at 37°C and Proteinase K at 59°C overnight. After hot phenol extraction with Trizol, the isolated LPS was run on a 16% Tricine gel. The gel was then stained using Pro-Q Emerald 300 Lipopolysaccharide Gel Stain Kit and imaged using UV light on a Protein Simple imager.

Antimicrobial susceptibility

Antimicrobial susceptibility testing of bacterial isolates were performed according to routine microbiology laboratory protocols using the Microscan automated system with the gram-negative panel, with additional E-testing as needed. Susceptibility breakpoints were derived from Clinical and Laboratory Standards Institute guide (Clinical and Laboratory Standards Institute, 2017).

Kinetic growth curves and static growth assays

For kinetic growth assays, isolates were grown to logarithmic phase in LB, normalized and inoculated (1:100) in a round-bottom 96-well plates with a final volume of 100 mL per well of LB, RPMI media or M9 salts with relevant supplements or antibiotics when indicated. Plates were incubated under agitation at 37°C overnight for kinetic growth curves. OD₆₀₀ was measured every 15-30 minutes for 18 hours on a SpectraMax M2 Microplate reader.

Static metabolite growth and biofilm assay

For static growth assays, bacteria supplemented M9 Minimal Media (MM) or LB were standardized to an OD₆₀₀ of 0.1, pelleted and washed twice with the respective media. Bacteria were incubated in a 1:100 dilution either in media alone or in media with increasing concentrations of specific metabolites or H₂O₂ in round-bottom 96-well plates with a final volume of 100 mL per well. Plates were incubated statically at 37°C overnight and the next day, OD₆₀₀ was measured on a Tecan Infinite 200. To measure biofilm formation, overnight cultures were standardized to an OD of 1, inoculated 1:100 in TS media + 0.5% glucose in a 96-well plate and grown statically overnight at 37°C. In the morning, the OD₆₀₀ was measured. After methanol wash, the wells were then stained with 1% crystal violet, resuspended with 33% acetic acid and the OD₅₄₀ was measured.

Single carbon source assimilation

Bacterial isolates were grown to exponential phase and normalized to an OD₆₀₀ of 0.5. Bacteria was then added to a PM1 Pheno-type Microarray, a 96-well plate array with a single carbon source in each well. The protocol provided by the manufacturer was strictly followed. Plates were incubated at 37°C for 24-48h.

Seahorse analyzer

A sensor cartridge was hydrated per the manufacturer's instructions overnight at 37°C. For bacteria alone, 10⁷ CFU was added to XF24 Cell Culture Microplates with XF base medium supplemented with 2mM glutamine. The extracellular acidification rate and oxygen consumption rate were measured using a XF24 Seahorse analyzer (Agilent). Each measurement cycle consisted of a mixing time of 3 minutes and a data acquisition period of 3 minutes, generating 12 data points over 73 minutes. Using the XF Glycolysis Stress Test Kit, Glucose (10 mM) was added to stimulate glycolysis, oligomycin (1 µM) to suppress oxidative phosphorylation and unleash glycolytic capacity, and 2-deoxyglucose (50 mM) to inhibit glycolysis.

Bacterial ROS production

Single colonies of KP35, Δatf3, Δatf3::atf3, and PAO1 were grown overnight in M9 MM supplemented with 62.5 mM glucose then subcultured (1:100) and standardized to OD₆₀₀ of 0.5, washed twice with and resuspended in M9 MM. The pellet was then stained

with MitoSOX for 20 minutes, before pelleting bacteria and washing twice with PBS. Dye intensity was then quantified on a BD FACS-Canto II.

ATP assay

Bacteria in logarithmic phase was standardized to OD₆₀₀ of 0.5 and resuspended to a concentration of 10⁸ CFU/mL. Equal portions of BacTiter-Glo Reagent was added to 100 mL bacterial suspension in white-walled 96-well plates. Contents were briefly mixed on a shaker for 5 minutes before recording luminescence on a SpectraMax M2 Microplate reader.

RNA-seq and qRT-PCR

Isolates were grown to mid/late log phase (OD₆₀₀ 0.5) in non-selective LB broth, pelleted, resuspended, and incubated in 50 mg/mL lysozyme in 50 μM Tris-HCl 10 μM EDTA pH 7.5 for 30 minutes at 37°C, followed by addition of TRK lysis buffer. After 10 minutes at room temperature, 70% ethanol was added and samples were transferred to the columns in the E.Z.N.A. Total RNA Kit I. RNA was isolated following the manufacturer's instructions and treated with DNase using the DNA-free DNA removal kit. To enrich mRNA content, rRNA was removed from isolated RNA using the MICROBExpress. For RNA-Seq, library prep of enriched mRNA was performed with the Truseq mRNA stranded kit, followed by sequencing using the 150 cycle v2 kit on an Illumina MiSeq. Quality-filtered reads (*Trimmomatic*) from all isolates were mapped against KP35, which was used as a reference genome. This was generated using Nanopore sequencing and hybrid assembly as previously described, using *Bowtie2* (Langmead and Salzberg, 2012). DESeq2 (Love et al., 2014) in R was used to identify the significantly up and/or downregulated mRNA transcripts using Benjamini-Hochberg p value adjustment to obtain FDR values (Creecy and Conway, 2015; Haas et al., 2012). The top 50 upregulated genes in WT KP35 over the Δatf3 mutant were analyzed using KEGG Mapper.

For confirmatory studies, isolated bacterial RNA transcribed to cDNA using a High Capacity cDNA Reverse transcription kit. Finally, qRT was performed using relevant primers and PowerSYBR Green PCR Master Mix on a StepOnePlus Real-time PCR System (Applied Biosystems), using StepOne Software. The ribosomal gene 16S was used as the house keeping gene and the ΔΔCT values were then calculated. The primer sequences used are presented in Table S1.

Cell lines

Seahorse analyzer

For studies using the Seahorse analyzer (Agilent), the media for plated THP-1 monocytes was replaced with XF base medium supplemented with 2 mM glutamine 1 hour prior to infection. The cells were then infected with the desired bacterial isolate at a MOI of 10 and incubated at 37°C without CO₂ for 3 hours. Measurements were then taken as described above.

Gentamicin protection assay

Differentiated and weaned THP-1 cells were infected with bacteria (MOI 10) for 30 minutes and then the media was replaced with RPMI + 10% HI FBS with Gentamicin 500 mg/mL. After 2 or 8 hours from the start of the infection, cells were recovered using TrypLE Express, lysed with saponin 0.2% and serial dilutions were plated on LB agar. An aliquot was set aside for cell enumeration and counted on a Countess (Invitrogen) with Trypan exclusion.

Mouse studies

In vivo experiments were performed using 8-week-old, male C57BL/6J mice. Mice were anesthetized with 100 mg/kg ketamine and 5 mg/kg xylazine given i.p. and infected intranasally with respective isolates (10⁸ CFU in 50 μL of PBS). Bacterial load of each compartment was quantified by serial dilutions on LB agar plates.

Competition experiment

Genomic DNA was extracted and purified from the BAL fluid or lung homogenate of C57BL/6J mice infected with KP35 or Δatf3 alone or 1:1, 1:5 or 1:10 ratios of KP35:Δatf3 *K. pneumoniae* using the QIAGEN DNeasy Blood and Tissue kit. Genomic DNA was diluted with nuclease-free water to 0.05 to 0.005 ng/μL. The presence of either KP35 or Δatf3 was measured by qPCR using Power SYBR Green Master Mix on the StepOne Real-Time PCR system (Applied Biosystems) with the primers listed below. Raw Ct values were standardized to house-keeping gene 16S and the proportion of either KP35 or Δatf3 was calculated.

atf3 Present FWD	ATG TGG GTG GAT TAT GCT AAG G
atf3 Absent FWD	ATG ATG AGT CTA GAA TGT TAT A
atf3 Common REV	GGC ATA TGG AAT GAA TAT ATA A

Histopathology and whole lung imaging

After euthanasia, tracheas were cannulated and lungs were inflated with Formalin Free Tissue Fixative at 5 cm of H₂O. Whole mouse lung was fixed with the same fixation solution for 24 hours, 70% ethanol for 24 hours, and then placed in paraffin blocks. H&E staining was performed in the usual fashion on 5 mm sections for gross pathology. Tissue sections were then digitally scanned using a Leica SCN400 whole slide digital imager.

Bronchoalveolar lavage fluid (BALF) assays

BALF was obtained by instilling aliquots of sterile PBS with calcium and magnesium into a cannulated trachea. Serial dilutions for bacterial enumeration were performed on the BALF prior to centrifuging. The supernatant of the first mL of BALF was set aside for cytokine array, 31-plex mouse discovery assay. The total cellular content was set aside for flow cytometry (FC).

Analysis of immune cell populations

To further delineate immune cell populations, analysis of cell populations in BALF or single cell suspension of lung homogenate was conducted using multi-color FC on a BD LSR II. Cells were labeled with a combination of PerCP-Cy5.5-labeled anti-CD11c, PE-Cy7-labeled anti-F4/80, phycoerythrin (PE)-CF594-labeled anti-Ly6C, BV510-labeled anti-CD11b, BV605-labeled anti-Ly6G, APC-Cy7-labeled anti-MHCII, AF700-labeled anti-CD45 and AF647-labeled anti-Siglec F. LIVE/DEAD Fixable Blue Dead Cell Stain Kit, for UV excitation and Fc block (anti-mouse CD16/32) was added to each sample.

Uniform dye microspheres were added to calculate the concentration of cellular components. All flow data was analyzed on FlowJo. Research reported in this publication was performed in the CCTI Flow Cytometry Core, supported in part by the Office of the Director, National Institutes of Health under award S10RR027050. The content is solely the responsibility of the authors and does not necessarily represent the official views of the National Institutes of Health.

Glucose assay on murine BALF

The glucose concentration in BALF from WT KP35 and $\Delta atf3$, and $\Delta atf3::atf3$ infected C57BL/J6 mice was determined using a colorimetric glucose assay kit. The glucose reaction mix was added to BALF samples and then read at OD₅₇₀ on a Tecan Infinite 200. A standard curve was generated to determine the final concentration of glucose in the BALF.

Targeted metabolomics

Targeted polar metabolomics were performed at the shared resource at Cornell University Medical Center, Metabolomics core on BALF harvested at multiple time points post inoculation and intracellular bacterial metabolites. For intracellular metabolites, bacteria were lysed with multiple freeze thaws cycles with liquid nitrogen and 100% ethanol with dry ice. Metabolites were extracted using 80% methanol. Targeted LC/MS analyses were performed on a Q Exactive Orbitrap mass spectrometer (Thermo Scientific) coupled to a Vanquish UPLC system (Thermo Scientific). The Q Exactive operated in polarity-switching mode. A Sequant ZIC-HILIC column (2.1 mm i.d. \times 150 mm, Merck) was used for separation of metabolites. The flow rate was set at 150 μ L/min. The buffers consisted of 100% acetonitrile for mobile A, and 0.1% NH₄OH/20 mM CH₃COONH₄ in water for mobile B. The gradient ran from 85% to 30% A in 20 min followed by a wash with 30% A and re-equilibration at 85% A. Metabolites were identified on the basis of exact mass within 5 ppm and standard retention times. Relative metabolite quantitation was performed based on peak area for each metabolite. PCA component analysis was performed using either MetaboAnalyst or independently generated R script.

Global acetylated lysine proteomics**Tissue lysis and in-solution digestion**

Overnight cultures were re-inoculated to an OD₆₀₀ 0.5 and washed with PBS^{-/-} \times 2. Bacterial cell pellets were lysed/homogenized by bead-beating in 8 M urea, 1% SDS, 200 mM EPPS (pH 8.5), and protease inhibitors. Lysates were cleared by centrifugation at 21,000 g for 30 min at 4°C, and the protein concentration was measured by bicinchoninic acid (BCA). Proteins were reduced with 5 mM tris(2-carboxyethyl)phosphine (TCEP), alkylated with 10 mM iodoacetamide (IAA), and quenched with 10 mM dithiothreitol (DTT). A total of 1 mg of protein was chloroform–methanol precipitated. Proteins were then reconstituted in 200 mM EPPS (pH 8.5) and digested by Lys-C overnight and trypsin for 6 h, both at a 1:50 protease-to-peptide ratio. Digested peptides were quantified using a Nanodrop at 280 nm, and 500 μ g of peptide from each sample were labeled with 800 μ g tandem mass tag (TMT) reagent using a 10-plex TMT kit (Navarrete-Perea et al., 2018). TMT labels were checked, 100 ng of each sample was pooled and desalted and analyzed by short SPS-MS3 method, and using normalization factor samples were bulk mixed at 1:1 across all channels and desalted using a 500 mg Sep-Pak solid-phase extraction column and dried using vacuum centrifugation.

Acetylated lysine peptides enrichment

Desalted dried isobaric labeled peptides (5 mg) were resuspended in 1.4 mL of ice-cold IAP buffer (50 mM MOPS (pH 7.2), 10 mM sodium phosphate and 50 mM NaCl) and centrifuged at maximum speed for 5 min at 4°C to remove any insoluble material. Supernatants (pH ~7.5) were incubated with the washed PTMScan® Acetyl-Lysine Motif [Ac-K] antibody beads for 2 hours at 4°C with gentle end-over-end rotation. After centrifugation at 2000 \times g for 1 min, beads were washed three times with ice-cold IAP buffer and three times with ice-cold HPLC water. The acetylated lysine peptides were eluted twice with 0.15% trifluoroacetic acid (TFA), desalted using a homemade SDB-RP StageTip, and dried via vacuum centrifugation.

LC-MS/MS analysis

The isobaric labeled, dried, acetylated lysine peptides were dissolved in 10 μ L of (3% acetonitrile/ 0.1% formic acid), and analyzed on an Orbitrap Fusion mass spectrometer coupled to a Dionex Ultimate 3000 (ThermoFisher Scientific) using the TMT-SPS-MS3 method (Jiang et al., 2017). Peptides were separated on an EASY-Spray C18 50cm column (Thermo Scientific). Peptides elution and separation were achieved at a non-linear flow rate of 250 nL/min using a gradient of 5%–30% of buffer B (0.1% (v/v) formic acid, 100% acetonitrile) for 110 minutes with a temperature of the column maintained at 50°C during the entire experiment. MS1 data were collected using the Orbitrap (120,000 resolution; maximum injection time 50 ms; AGC 4 \times 10⁵). Determined charge states between 2 and 5 were required for sequencing and a 45 s dynamic exclusion window was used. Data-dependent top10 MS2 scans

were performed in the ion trap with collision-induced dissociation (CID) fragmentation (Turbo; NCE 35%; maximum injection time 50 ms; AGC 1×10^4). MS3 quantification scans were performed using the multi-notch MS3-based TMT method (ten SPS ions; 50,000 resolution; NCE 65%, maximum injection time 105 ms; AGC 1×10^5) using the Orbitrap.

Data analysis

Raw mass spectrometric data were analyzed using MaxQuant to perform database search and TMT reporter ions quantification. TMT tags on lysine residues and peptide N termini (+229.163 Da) and the carbamidomethylation of cysteine residues (+57.021 Da) was set as static modifications, while the oxidation of methionine residues (+15.995 Da), deamidation (+0.984) on asparagine and glutamine and acetyl (+42.010 Da) on lysine were set as a variable modification. Data were searched against the KP35 database with peptide-spectrum match (PSMs) and protein-level FDR at 1% FDR. Acetylated lysine peptides identification and quantification were imported into GraphPad Prism for t test statistical analysis (FDR < 0.05) to identify proteins demonstrating statistically significant changes in abundance.

QUANTIFICATION AND STATISTICAL ANALYSIS

Statistics

All statistical analysis was performed using GraphPad Prism Version 8.4.0 (February 20, 2020). For most datasets, either a one-way or two-way ANOVA was performed with post test analysis for multiple comparisons. For datasets in which only two datasets could be compared, two-tailed Mann-Whitney test was performed. For larger datasets (metabolome and acetylome), multiple t tests with a FDR at 1% was used. A p value of < 0.05 was considered significant. Grubb's test was performed on all datasets to remove significant outliers with an α value of 0.05. Experiment specific tests, exact value of n and what it represents, and definition of center and dispersion are described in the individual figure legends. Power calculations were performed *a priori* for the *in vivo* experiments. The animals were randomized to groups at random and no mice were excluded.